Entangled two-photon quantum heat engine: Dissipative nonequilibrium dynamics and correlated statistics

JunJie Chen [1] and Konstantin Dorfman [1,2,3,*]

[1]*State Key Laboratory of Precision Spectroscopy, East China Normal University, Shanghai 200241, China*
[2]*Center for Theoretical Physics and School of Sciences, Hainan University, Haikou 570228, China*
[3]*Himalayan Institute for Advanced Study, Unit of Gopinath Seva Foundation, MIG 38, Avas Vikas, Rishikesh 249201, Uttarakhand, India*

Recently, the thermodynamics of open quantum systems driven by light fields has been investigated in the framework of quantum heat engines, whose output work can be measured as a spectroscopic signal. In this work, we investigate a four-level quantum heat engine that generates cascaded entangled photon pairs, treating the hot bath as an incoherent thermal pump and focusing on the correlation statistics of the output work and photon indistinguishability. We show that the dissipative nonequilibrium dynamics of this thermodynamic open quantum system can be reconstructed by correlation measurements under carefully mediated optical control. Comparing our findings with the traditional coherently pumped model, we find that the thermal pumping has the potential to generate nonclassical correlations resulting in photon indistinguishability, displaying an advantage in probing the nonequilibrium effects induced by the baths at different temperatures. Our work also demonstrates that incoherent pumping can optimize such correlations in output work beyond the classical limit. Lastly, we show that nonclassical correlations and resonant power at steady state cannot be simultaneously maximized in the weak coupling regime.

I. INTRODUCTION

Numerous aspects of quantum science and technology benefit from the properties of photons, e.g., quantum entanglement [1–5], photon antibunching [6–9], etc. In the field of optical spectroscopy [10], entangled photon pairs demonstrate the capacity to excite atomic and molecular systems with higher signal at lower intensities yielding linear scaling for the two-photon absorption [11,12], and to control exciton distributions in complex systems [13]. The entangled photon pairs can be further utilized to control the population of vibronic excited states and to investigate internal conversion processes [14]. The use of complex atoms and molecules in generating and mediating the quantum properties of light, such as entanglement and antibunching, usually requires both the consideration of optical control as the common framework in description of quantum states of light and its interactions with open quantum systems containing environmentally controlled degrees of freedom [15]. This suggests a strong connection between optical control methods and the framework of open quantum systems.

A quantum heat engine (QHE) [16,17] is a thermodynamic manifestation of open quantum systems [15,18,19]. It can be regarded as a miniature version of the classical heat engine on the scale where quantum effects cannot be neglected [20]. In the last few decades, research on QHEs attracted considerable interest due to its connection to real physical systems, such as lasers [21], solar cells [22–24], and biological systems [25]. Phenomena of profound quantum nature, such as quantum coherence [25–28] and entanglement [29–32], and their effects on the performance of QHEs have been further investigated in the steady state. Meanwhile, novel topics such as quantum statistics of QHE [33] have recently attracted significant attention. Recent experiments demonstrated that the physics of QHEs [34,35] can be studied using optical pump-probe setups [36] and the radiation resonantly driving the electronic transitions in the material systems can be seen as a working fluid. It has further been shown [37] that the dynamics of open quantum systems driven by a coherent pump followed by relaxation dynamics can be replaced by an effective thermal bath. The spectroscopic setup can be therefore interpreted as the QHE, which transfers energy from one thermal bath (pump pulse) to another (probe pulse). Therefore, QHEs can be studied under the framework of spectroscopy where the work output is measured as a spectroscopic signal of the probe, establishing a link between spectroscopy and quantum thermodynamics in and out of equilibrium.

In this paper, we explore a four-level quantum heat engine that generates a cascade of entangled photon pairs by treating the hot bath as an incoherent thermal pump. Our focus is on the correlation statistics of the output work and the indistinguishability of the cascaded entangled photon pairs commonly indicated by the Hong-Ou-Mandel (HOM) dip [38] in the photon coincidence counting. Note that the correlation statistics of the output work is equivalent to the photon correlation statistics of the cascaded entangled photon
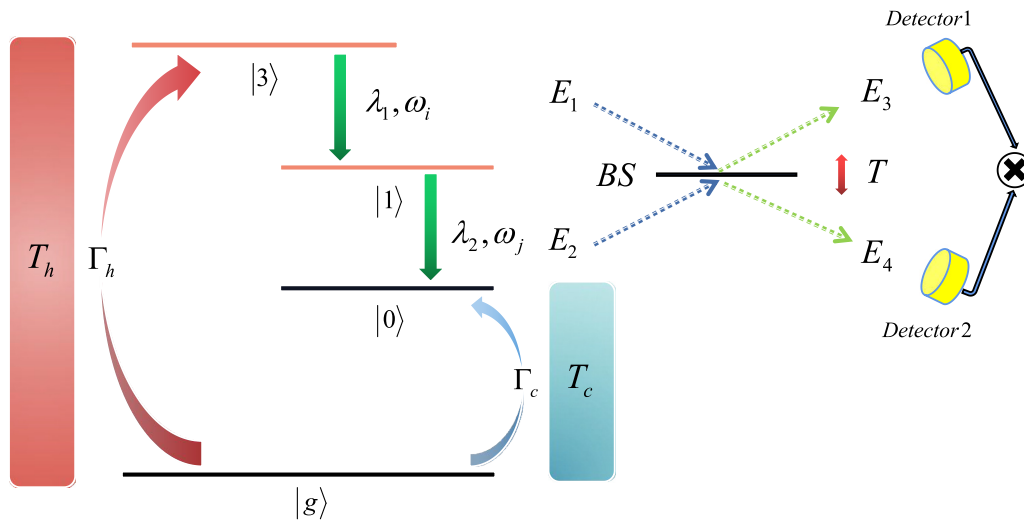
*dorfmank@hainanu.edu.cn

FIG. 1. Four-level QHE with the transitions g-3 and g-0 driven by the two heat baths with the hot temperature T_h and the cold temperature T_c, respectively. The two-photon cascaded emission occurs between the energy levels 3 and 0 via the intermediate level 1. A beam splitter and the two detectors are added to produce and examine the correlation and the distinguishability of two output photons using coincidence measurements.

pairs, and both of them can be characterized by the photon coincidence counting in the correlation measurements [39]. Two gated detectors are introduced to perform the optical signal detection in the quantum regime. We demonstrate that the photon coincidence counting with carefully mediated central times of the temporal gates, along with the gated detection, can be used to reconstruct the dissipative nonequilibrium dynamics of the thermodynamic open quantum system. Our results provide a novel way to characterize nonequilibrium dynamics through correlation measurements.

Further, we compare the findings with the coherently pumped model commonly used in parametric down conversion [40] by replacing the hot bath by a resonant interaction with a coherent laser. Our comparison reveals that the thermal pumping has the potential to generate nonclassical correlations (nontrivial peaks) in the output, leading to photon indistinguishability. This highlights the thermodynamic advantage of thermal pumping in showcasing the nonequilibrium effects induced by the baths at different temperatures, which does not exist in the coherently pumped model. Our research expands the investigation of two-photon process to include both nonequilibrium and steady-state regimes, and also demonstrates that a specific parameter regime for the incoherent pumping has the potential to optimize the instantaneous correlations in the output work, surpassing the classical boundaries in the time domain.

By examining the incoherently pumped QHE at steady state, we finally show that resonant power output and nonclassical correlations (nontrivial peaks) cannot be simultaneously maximized.

The paper is organized as follows. In Sec. II, we introduce the model of the two-photon cascade QHE pumped by the incoherent thermal pump. We present the master equation, calculate the photon coincidence signal, and discuss the approximations involved, as well as the methods to recover the dissipative population dynamics from the signal. We also discuss the power at the resonant frequency and its connection

with the nonclassical correlations (nontrivial peaks) in this section. In Sec. III, we present and discuss the coherently pumped two-photon cascade model. The comparison of the two models and conclusions are given in Sec. IV.

II. INCOHERENTLY PUMPED QHE MODEL

A. QHE model and photon counting setup

We consider a four-energy-level system shown in Fig. 1, the ground state g and the excited states 0, 1, 3 with energies ordered as $e_0 < e_1 < e_3$. A hot bath with temperature T_h drives the g-3 transition incoherently. A cascade of two photons is generated from the higher excited state 3 to the lower state 0 via the intermediate state 1. The system then undergoes the transition from 0 to g via the contact with the heat bath with low temperature T_c. Following Ref. [37], we treat the hot bath as an incoherent thermal pump field and the two-photon cascade emission as the probe signal is equivalent to the work of the QHE.

Following the Hong-Ou-Mandel (HOM) experiments [38], we add the 50:50 beam splitter (BS) to separate the cascading two photons that are subsequently registered by time-frequency detectors 1 and 2. There are two types of possible outcomes for the BS: two output photons are registered in a single detector (1 or 2) or the coincidence event where one output photon is detected in each detector. The ratio among these outcomes reflects the Bose-Einstein statistics and the degree of the photon distinguishability. If the two output photons incident on the beam splitter are indistinguishable, the photon coincidence counting (PCC) signal [39] vanishes. This is known as the HOM dip. Varying the position of the beam splitter introduces a delay T between the two photons.

Temporally and spectrally resolved measurements have proven to be valuable in extracting important information about matter [41,42]. The independent control of time and frequency gating parameters further enhances our ability to manipulate output signals [43]. Specifically, the central time

parameter corresponds to the resolution time of a temporal gate, which can be used to capture the temporal features of output signals. For instance, by adjusting the gating bandwidths and the central times of temporal gates, one can effectively capture and study nonequilibrium and nonstationary states of matter [43]. Moreover, the control of central times and bandwidths of temporal gates allows us to investigate photon correlation statistics and two-photon interference. In Ref. [39], the photon correlation statistics and position of the HOM dip can be characterized by the central times t_s and t_r, which reveals the quantum interference effect in the time domain.

In our research, we leverage the central times of the temporal gates t_{c1} and t_{c2} to expand the study of the two-photon physics to both nonequilibrium and steady-state regimes. First, we employ the t_{c1} and t_{c2} to investigate the temporal correlation statistics and determine the position of the HOM dip, which reveals the quantum interference effect in the time domain. Additionally, by manipulating the central times and bandwidths, we can reconstruct the nonequilibrium dynamics of the system under specific optical control. This approach enables us to capture and characterize the nonequilibrium effects associated with the two-photon generation process in the time domain. It is important to note that the two-photon generation process is inherently nonequilibrium, and controlling the central times is crucial for understanding and analyzing the corresponding nonequilibrium effects.

Along with the central times of the temporal gates t_{c1} and t_{c2}, we obtain the set of control parameters that allows us to display the HOM dip in the time domain. We next introduce the relative PCC signal [39,44], whose normalized value at the dip is related to the visibility of the measurement. The relative PCC rate varies between 1 for completely distinguishable photons and 0 when they are totally indistinguishable. For classical fields and 50:50 beam splitters, the relative PCC rate cannot be less than 1/2. We therefore denote the photons to be indistinguishable (distinguishable) if the relative PCC rate is smaller (larger) than 1/2.

Note that in certain cases, the asymptotic value ($t_{c1}, t_{c2} \to \infty$ corresponding to the steady-state regime) that is conventionally used to normalize the relative PCC does not represent the actual maximum value of the PCC due to nonequilibrium dynamics, which may change the shape of the PCC dip. In this case the visibility and the dip normalization have to be redefined to account for the nonequilibrium dynamics and quantify the indistinguishability of the two detected photons.

The light-matter dynamics in the interaction picture can be described by the master equation (see Appendix A):

$$\frac{\partial \rho}{\partial t} = \frac{-i}{\hbar}[H_{\text{int}}(t) + H_s, \rho] + \mathcal{L}_c[\rho] + \mathcal{L}_h[\rho]. \quad (1)$$

The joint density matrix of the interacting system plus the probe fields is represented by $\rho(0) = \rho_s(0) \otimes \rho_{f1}(0) \otimes \rho_{f2}(0)$ at the initial moment, and the system is in the ground state. The two multimode probe fields are in the vacuum state initially. Here, H_s represents the system Hamiltonian, and H_{int} denotes the weak probe fields-system interaction. $\mathcal{L}_c[\rho]$ and $\mathcal{L}_h[\rho]$ represent the Liouville operators describing the dissipative dynamics due to the contact with the cold and the hot temperature baths in the framework of the

Weiskopf-Wigner theory [26,45], respectively. The PCC signal characterizes the correlation statistics of the output, and is defined as a normally ordered four-point correlation function of the time-and-frequency gated electromagnetic field operators $\hat{E}_3$ and $\hat{E}_4$ incident on the detector:

$$R^{34}(\alpha_3, \alpha_4) = \int_{-\infty}^{\infty} dt_s \int_{-\infty}^{\infty} dt_r \langle \hat{E}_{3tf}^\dagger(t_r)\hat{E}_{4tf}^\dagger(t_s)$$
$$\times \hat{E}_{4tf}(t_s)\hat{E}_{3tf}(t_r)\rangle, \quad (2)$$

where $\langle \ldots \rangle = \text{tr}(\ldots \rho)$ is the trace with respect to the total density operator, α_3 and α_4 represent the detectors' parameters. The output ($\hat{E}_3$, $\hat{E}_4$) and the input ($\hat{E}_1$, $\hat{E}_2$) fields are related by:

$$\hat{E}_3(t) = \frac{\hat{E}_1(t) - i\hat{E}_2(t + T)}{\sqrt{2}}, \hat{E}_4(t) = \frac{\hat{E}_2(t) - i\hat{E}_1(t - T)}{\sqrt{2}},$$
$$(3)$$

where c is the speed of light and cT is a small difference in the path length of the two arms. Here we note the delay time T can be both positive or negative. The time-and-frequency gated field operators are defined as [43]:

$$\hat{E}_{3,t_{c1},\overline{\omega_1}}(t'') = \int_{-\infty}^{\infty} dt' F_{f1}(t'' - t', \overline{\omega_1})F_{t1}(t', t_{c1})\hat{E}_3(t'),$$

$$\hat{E}_{4,t_{c2},\overline{\omega_2}}(t'') = \int_{-\infty}^{\infty} dt' F_{f2}(t'' - t', \overline{\omega_2})F_{t2}(t', t_{c2})\hat{E}_4(t'). \quad (4)$$

Here, t_{ci}, $\overline{\omega_i}$, F_{fi}, F_{ti} ($i = 1, 2$) represent the central time and frequency of the detectors, the frequency and time gating functions, respectively.

By solving the master equation for the density matrix elements, one can thus calculate the time-and-frequency gated PCC signal. For simplification, here we give the compact result when $T < 0$:

$$R^{34}(t_{c1}, t_{c2}) = U_1(t_{c1}, t_{c2}) + U_2(t_{c1}, t_{c2}),$$

$$U_1(t_{c1}, t_{c2}) = \frac{M_1 + (M_2 + M_3)\theta(t_{c2} - t_{c1})}{8[1 + 2n_h + n_c(2 + 3n_h)]\sigma_{T2}},$$

$$U_2(t_{c1}, t_{c2}) = \frac{M_4 - r_4 M_5 - r_3 M_6 + r_4 M_7 + r_3 M_8 - M_9}{8[1 + 2n_h + n_c(2 + 3n_h)]}.$$
$$(5)$$

Note that n_h and n_c are the average photon occupation numbers for the hot bath and the cold bath, respectively, given by: $n_h = \{\exp[\hbar\omega_{3g}/(k_B T_h)] - 1\}^{-1}$, $n_c = \{\exp[\hbar\omega_{0g}/(k_B T_c)] - 1\}^{-1}$. The remaining parameters and the detailed result are given in Appendix B and C.

B. Relative PCC for the incoherently pumped QHE

We first note that the signal $R^{34}(t_{c2})$ for a fixed t_{c1} depends on the sign of T as shown in Figs. 2(a), 2(b). Here, σ_{T1} and σ_{T2} are the corresponding bandwidth of the temporal gates (see Appendix B). One can find that the ratio between the dip value and the maximum value for $T < 0$ is apparently smaller than if $T > 0$.

The reason can be similarly explained using the argument presented in Ref. [46]. The degree of the entanglement between the two cascaded photons is closely related to the
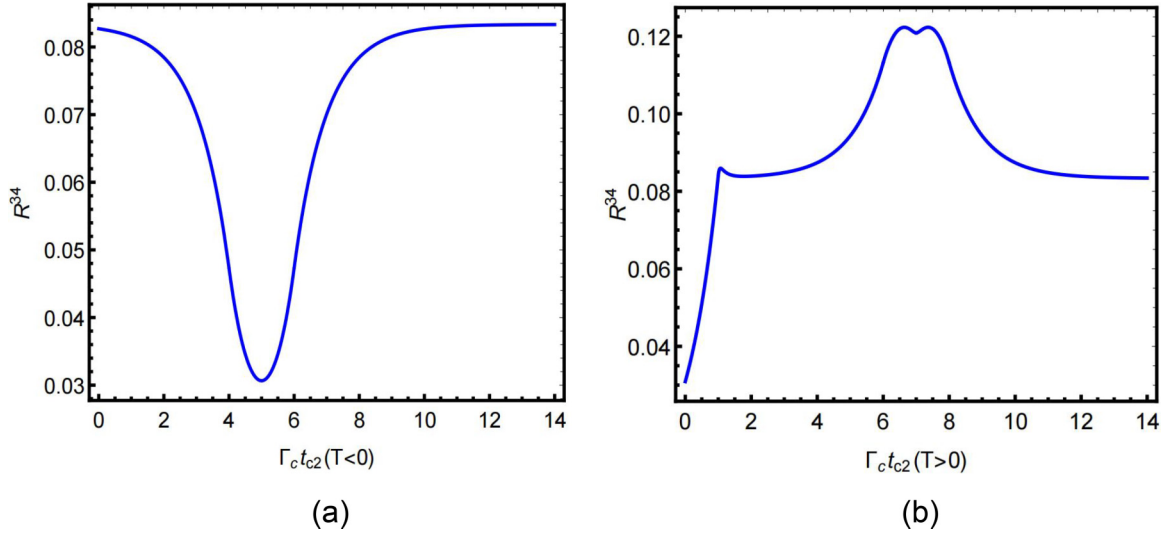
FIG. 2. The simplified detected PCC signal R^{34} in Eq. (2). The parameters used in the simulations are scaled with Γ_c such that: $\Gamma_h = 2\Gamma_c$, $\sigma_{T1} = \sigma_{T2} = \Gamma_c$, $n_c = 4$, $n_h = 6$, $t_{c1} = 6/\Gamma_c$, $|T| = 1/\Gamma_c$, (a) $T < 0$, (b) $T > 0$.

causality of time-ordered emission in the time domain, i.e., the photon 2 is followed by the photon 1 in the time domain due to the constraint of energy level transition 3-1-0. The time-domain detection of photon 2 follows the detection of photon 1 when the two photons obey the temporal causality, resulting in the entanglement erosion [15]. However, when the emission times for the two photons are nearly indistinguishable, which means the temporal causality is nearly eroded, the corresponding entanglement is largely enhanced. Briefly, breaking the causality of time-ordered emission in the time domain can strengthen the entanglement between the two cascaded photons.

For the fixed time of the given output in Eq. (3) at $T < 0$, the collected photon 1 corresponding to the electric field E_1 is generated later than the collected photon 2 induced by the field E_2, which means the two photons break the causality of time-ordered emission in the time domain and thus have high degree of entanglement. Obviously, the break of the temporal causality is due to the existence of delay time $T < 0$. In the opposite case where $T > 0$, one can clearly see the temporal causality is strengthened, which reduces the entanglement of the two photons. Thus, we can find that ratio between the dip value and the maximum value for $T < 0$ is apparently smaller than that if $T > 0$ in Fig. 2, which means the non-classical features of the two-photon state at $T < 0$ are much more pronounced compared to $T > 0$. According to the above discussion and also for simplicity, we will only consider the case where $T < 0$ in the subsequent analysis.

By setting t_{c1}, t_{c2} to infinity, one can obtain the steady-state value for the detected signal. Note that the steady-state value for the PCC signal when $T < 0$ is proportional to the steady-state value of $\rho_{33}(\infty)$, which justifies the steady-state parameter regime for the detection signal. The relative PCC signal can be introduced in the further analysis and defined as:

$$G^{(2)}(t_{c1}, t_{c2}) = \frac{R^{34}(t_{c1}, t_{c2})}{R^{34}(\infty, \infty)},$$

$$R^{34}(\infty, \infty) = \frac{(1 + n_c)n_h}{4[1 + 2n_h + n_c(2 + 3n_h)]\sigma_{T1}\sigma_{T2}}. \quad (6)$$

Figure 3(a) shows that at fixed t_{c1} the relative PCC has a dip as a function of t_{c2} reaching the value of 0.82, which corresponds to the regime of distinguishable photons. For smaller temporal gate bandwidth, detectors can accumulate more photons arriving at different times, which can be distinguished due to higher probability of antibunching. With the increase of the detector bandwidth, less photons are accumulated and the bunching properties become important. Thus, the dip minimum is reduced to 0.68 in Fig. 3(b), and further down to 0.43 in Fig. 3(c), which emerges as the regime for indistinguishable photons with value 0 for the HOM dip reached in the limit of infinitely large gating bandwidth.

C. Set of approximations to determine the dip position and its value

In order to determine the precise position of the HOM dip, we need to establish a set of approximations for the steady-state detection when $T < 0$:

(i) We assume both detectors have the same bandwidth $\sigma_{T1} = \sigma_{T2}$, and set $|T| < \Gamma_c^{-1}$ in the further analysis of the incoherently pumped model.

(ii) We vary t_{c2} while the t_{c1} remains fixed by setting its value $t_{c1} \gg \max\{\frac{1}{l_2}, \frac{1}{l_3}\}$, which also reduces the nonequilibrium effect of the system related to t_{c1}. The dynamic factors l_2, l_3 are defined in Appendix C, characterizing the combined driving nonequilibrium dynamical effects caused by both the hot and the cold baths in the time domain.

Under the above approximations, one can use Eq. (6) to find the precise position of the dip determined by:

$$t_{c1} - t_{c2} = -T. \quad (7)$$

Note that Eq. (7) is independent of the open quantum system's parameters, which characterizes the steady-state. Using Eqs. (6) and (7), one can find the value of relative PCC signal at the dip in the steady-state regime for $t_{c1} \gg \max\{\frac{1}{l_2}, \frac{1}{l_3}\}$ given by:

$$D_{\text{inc}}^{\text{ss}} \equiv \min G^{(2)}(t_{c1}, t_{c2}) = G^{(2)}(t_{c1} - t_{c2} = -T) = e^{T\sigma_{T2}}. \quad (8)$$
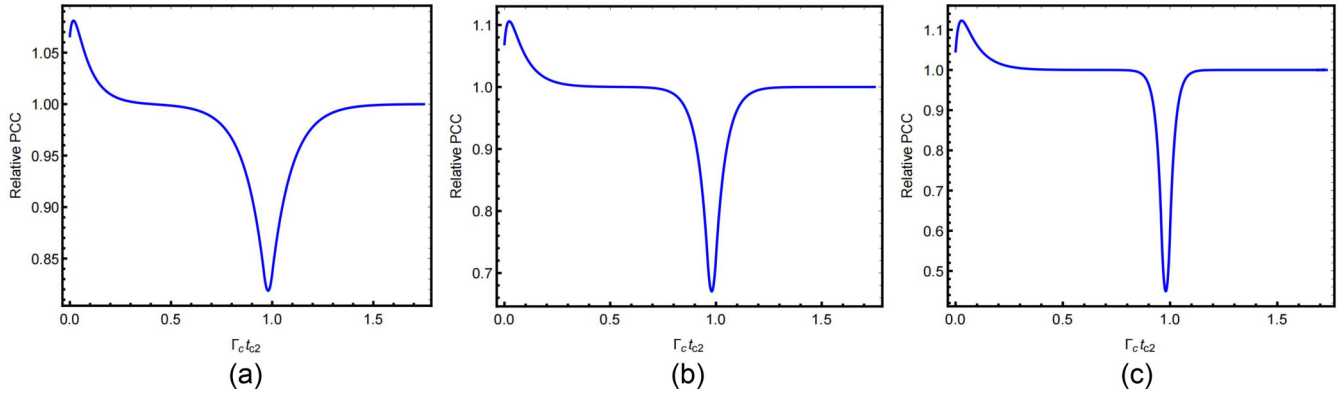
FIG. 3. The relative PCC signal in Eq. (6) vs t_{c2} at fixed t_{c1} for the different time detector bandwidth scaled with Γ_c. (a) $\sigma_{T1} = \sigma_{T2} = 10\Gamma_c$, (b) $\sigma_{T1} = \sigma_{T2} = 20\Gamma_c$, (c) $\sigma_{T1} = \sigma_{T2} = 40\Gamma_c$. The fixed parameters for the simulations are $\Gamma_h = 2\Gamma_c$, $n_c = 4$, $n_h = 6$, $t_{c1} = 1/\Gamma_c$, $T = -0.02/\Gamma_c$.

The relative PCC signal $G^{(2)}$ at fixed t_{c1} with large detector bandwidth and small $|T|$ is shown in Fig. 3(c). The position and the value of the dip, which constitute the first-order effect, depend on the details of the detection setup such as t_{c1}, t_{c2}, T, and the detector bandwidth, but not on the details of the thermodynamic open quantum system and its dynamics. As has been previously shown, the details of the system enter into the spectral linewidth of the resonance peaks [39]. The precise determination of the width is more subtle and constitutes the second-order effect, which is out of the scope of the present work. At the same time, a first-order effect still exists that allows monitoring of the system dynamics, which will be discussed below.

D. Reconstructing the system dynamics using the probe signal

In Fig. 3, we note the following detail: in addition to the single dip structure, which emerges from the steady-state level, the $G^{(2)}$ signal also contains a nontrivial peak at short t_{c2} reaching the value of 1.12. This peak value is much larger than the steady-state value. As we will discuss later, this can be shown as a dynamical signature of open quantum system features, and therefore, the detailed analysis of the peak can recover the dynamical properties of the system and its interaction with the joint heat temperature baths.

In order to quantify the possible peak position and its magnitude, we first note that the peak will occur at short time t_{c2} long before the dip in the time domain. Thus in the following discussion related to the peak, we will focus on the temporal properties of the PCC signal before the dip happens. Since we only want to see the nonequilibrium effect introduced by the system dynamics and exclude the time-delay effect brought by the beam splitter, we can set $T\{l_2, l_3\} \approx 0$. Assuming $t_{c1} \gg t_{c2}$ and taking $\sigma_{T2} \gg \max\{l_2, l_3\}$ that corresponds to the time-domain resolution regime for capturing system dynamics with precision, one can obtain:

$$G'^{(2)}(t_{c2}) = 1 - \frac{r_4 e^{-l_2 t_{c2}}}{2n_h(1+n_c)} - \frac{r_3 e^{-l_3 t_{c2}}}{2n_h(1+n_c)}. \quad (9)$$

On the other hand, we can further solve the density matrix equation in Eq. (1) perturbatively to obtain the dissipative nonequilibrium dynamics of $\rho_{33}(t)$ (see Appendix C), and then we can define:

$$\rho^{\text{inc}}(t) \equiv \frac{\rho_{33}(t)}{\rho_{33}(\infty)} = 1 - \frac{1}{2n_h(1+n_c)}(r_3 e^{-l_3 t} + r_4 e^{-l_2 t}),$$

$$\rho_{33}(\infty) = \frac{n_h(1+n_c)}{1 + 2n_c + 2n_h + 3n_c n_h}, \quad (10)$$

which establishes the relationship between the PCC signal and system dynamics as:

$$G'^{(2)}(t) = \rho^{\text{inc}}(t). \quad (11)$$

Thus, the system dynamics via $\rho_{33}(t)$ can be explicitly detected by the PCC signal. After defining the relative peak value as the maximum value of the population $\rho_{33}(t)$ relative to its steady-state value: $Q \equiv \frac{\max_t \rho_{33}(t)}{\rho_{33}(\infty)} = \max_t \rho^{\text{inc}}(t)$, we also define the maximum PCC value relative to its steady-state value: $Q^{\text{pcc}} \equiv \max_t G'^{(2)}(t)$. One can clearly note $Q^{\text{pcc}}_{\max} \leqslant Q_{\max}$ and the bound of $Q^{\text{pcc}}_{\max}$ can be achieved when $\sigma_{T2} \gg \max\{l_2, l_3\}$, corresponding to Eq. (9) and the time-domain resolution regime for accurately capturing system dynamics.

If $n_c \neq 0$, we only consider the high-temperature regime corresponding to the case $n_h > n_c \gg 1$. Thus, a relative peak value exists in Eq. (10) and is reached at time: $t' = \frac{\ln\left(\frac{-l_2 r_4}{l_3 r_3}\right)}{l_2 - l_3}$ with the corresponding value as the Q value:

$$Q = 1 - \frac{r_4\left(\frac{-l_2 r_4}{l_3 r_3}\right)^{-\frac{l_2}{l_2-l_3}} + r_3\left(\frac{-l_2 r_4}{l_3 r_3}\right)^{-\frac{l_3}{l_2-l_3}}}{2n_h + 2n_c n_h}. \quad (12)$$

Considering further a strong pump and high-temperature limit regime as: $n_h \Gamma_h \gg n_c \Gamma_c \gg \Gamma_h > \Gamma_c$, $n_h \gg n_c \gg 1$, the spontaneous emission can be neglected and the coefficients are reduced to: $r_4 \approx -n_c n_h$, $r_3 \approx 3n_c n_h$, $l_2 \approx 3\Gamma_c n_c$, $l_3 \approx 4\Gamma_h n_h$. Therefore, Eq. (12) is reduced to:

$$Q \approx 1 + 2^{-1-\frac{3\Gamma_c n_c}{2\Gamma_h n_h}}\left(\frac{\Gamma_c n_c}{\Gamma_h n_h}\right)^{\frac{3\Gamma_c n_c}{4\Gamma_h n_h}} - \frac{3\Gamma_c n_c}{8\Gamma_h n_h}. \quad (13)$$

By setting $x = \frac{\Gamma_c n_c}{\Gamma_h n_h}$ as a variable, we plot $Q(x)$ in Fig. 4. Thus, the relative peak value Q is maximized at $x = 0$
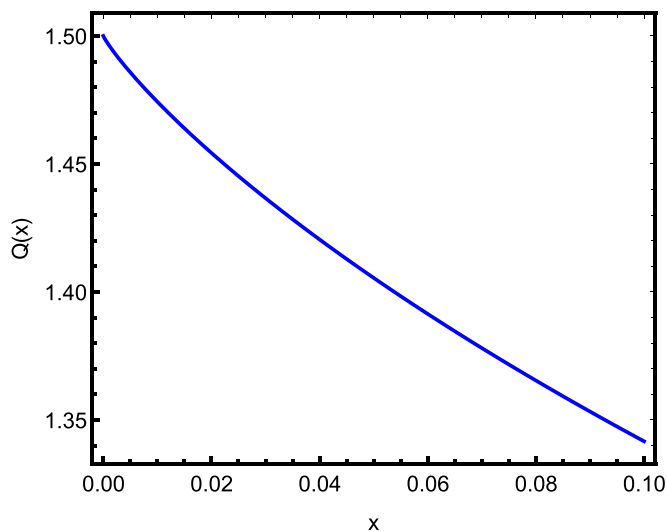
FIG. 4. Relative peak value $Q(x)$ for $x = \Gamma_c n_c / (\Gamma_h n_h)$ when we consider a strong pump and high temperature limit regime as $n_h \Gamma_h \gg n_c \Gamma_c \gg \Gamma_h > \Gamma_c, n_h \gg n_c \gg 1$.

corresponding to $Q_{\max} = 1.5$, which is a dynamical effect caused by the competition between the two baths. The nonequilibrium dynamics induced by the two baths can be understood as the dynamical process of the system where each bath tries to draw the system state closer to its respective thermal state [18]. In other words, each bath tries to drive the system according to its own temperature, but, unless all temperatures are equal the system can no longer be described by a canonical ensemble with respect to a single temperature. The system thus attempts to find a compromise between the different temperatures involved, which leads to the steady state with different temperatures. A typical example is the steady-state value of $\rho_{33}(\infty)$ in Eq. (10).

Due to the significant difference in driving effect between the two heat baths at short times, the system is mainly affected by the hot bath and the effect of the cold bath is relatively unimportant under our high-temperature limit condition resulting in $\rho_{33}(t) \to 0.5$. This also means the local steady state at the strong pump is rapidly reached only at the g-3 transition. But after a period of time, the existence of the cold bath plays an important role since the system is jointly driven by the two baths, which leads to $\rho_{33}(t) \to 1/3$ in the steady state and the existence of the relative nontrivial peak. In the high-temperature limit, we can clearly see $\max_t \rho_{33}(t) = 0.5$ and $Q \equiv \frac{\max_t \rho_{33}(t)}{\rho_{33}(\infty)} = 1.5$, which corresponds to our above analytical analysis.

Following the above discussions, the range of the peak in detected relative PCC signal is $1 \leqslant Q^{\mathrm{pcc}} \leqslant 1.5$ for the incoherently pumped QHE. We should emphasize the maximum value of the peak can be detected under the high-temperature limit assumption and the time-domain resolution regime: $\sigma_{T2} \gg \max\{l_2, l_3\}$. In the limit regime of photon distinguishability (small σ_T), the value of the peak signal will be reduced to the steady-state background.

If $n_c = 0$, Eq. (10) can be simplified as $\rho^{\mathrm{inc}}(t) = 1 - e^{-t(1 + 2n_h) 2\Gamma_h}$. This is an increasing function and the maximum value can be found when $t \to \infty$, corresponding to the

steady-state value. This means $Q = \max_t \rho^{\mathrm{inc}}(t) = 1$, which also leads to $Q^{\mathrm{pcc}} = 1$. The population of level 3 approaches a value dictated only by the hot bath, which is why there are absent of the nonclassical correlations (nontrivial peaks), since the cold bath, at zero temperature, is not competing for level 3.

In addition to the HOM dip and the peak due to the nonequilibrium system dynamics and in order to characterize the visibility for fixed t_{c1}, we introduce the dynamical visibility parameter V_{inc} defined by:

$$V_{\mathrm{inc}} \equiv \frac{\mathrm{dip}}{\max R^{34}(t_{c2})} = \frac{\mathrm{dip}}{R^{34}(\infty, \infty)} \frac{R^{34}(\infty, \infty)}{\max R^{34}(t_{c2})} = \frac{D_{\mathrm{inc}}^{\mathrm{ss}}}{Q^{\mathrm{pcc}}}. \tag{14}$$

If $n_c \neq 0$, we follow our detection protocol and only consider the high-temperature limit condition $n_h \gg n_c \gg 1$ and $T < 0$, which results in $V_{\mathrm{inc}} = \frac{e^{T\sigma_{T2}}}{Q^{\mathrm{pcc}}}$. Since $1 \leqslant Q^{\mathrm{pcc}} \leqslant 1.5$, it is clear that $e^{T\sigma_{T2}} \geqslant V_{\mathrm{inc}} \geqslant \frac{2e^{T\sigma_{T2}}}{3}$ with the lowest bound achieved in the high-temperature limit and the time-domain resolution regime: $\sigma_{T2} \gg \max\{l_2, l_3\}$. In the opposite limit when $n_c = 0$, the steady-state background fully defines the visibility and $V_{\mathrm{inc}} = D_{\mathrm{inc}}^{\mathrm{ss}} = e^{T\sigma_{T2}}$.

The above results suggest that the strong high-temperature thermal pumping has the potential to lead to higher degree of nonclassical correlations (nontrivial peaks) in the output, thereby enhancing the photon indistinguishability, while simultaneously highlighting the nonequilibrium effects of the dynamics induced by the two heat temperature baths in the incoherently pumped QHE system. This dynamics can be interpreted as a competition between the two temperature baths interacting with the system. Equation (11) suggests that the correlation measurement method provides a potential tool to give insight into the dynamic characteristics of the system. Additionally, the above discussions also demonstrate that the carefully tailored incoherent pumping has the potential to optimize the instantaneous correlations in the output work beyond the classical limit.

E. QHE power at the resonant frequency in the weak coupling regime

Traditionally, the QHE physics focuses on the maximization of the power or efficiency at maximum power [22,26], rather than looking at the correlations in the output work. In this section, we shift our focus from the correlation statistics of the output work to the steady-state power in the incoherently pumped QHE. Especially, we examine the ability of the QHE to produce steady-state power at the resonant frequency in the weak coupling regime [29]. Note that the correlation statistics is actually obtained in the same weak coupling regime as in the previous discussions.

A scheme depicting the production of output power is shown in Fig. 5(a), where two weak quantum single-mode probe fields E_a, E_b drive the respective transitions $3 \to 1$ and $1 \to 0$ resonantly. Corresponding to the previous discussions, the two probe fields are assumed to be in the vacuum state initially. Under these conditions, the fields and the system-fields interaction Hamiltonians are given by: $H_{f_1} = \hbar \omega_a \hat{a}^\dagger \hat{a}$; $H_{f_2} = \hbar \omega_b \hat{b}^\dagger \hat{b}$; $H_{\mathrm{int}} = \hat{E}_a^\dagger V_a + \hat{E}_a V_a^\dagger + \hat{E}_b^\dagger V_b + \hat{E}_b V_b^\dagger$,
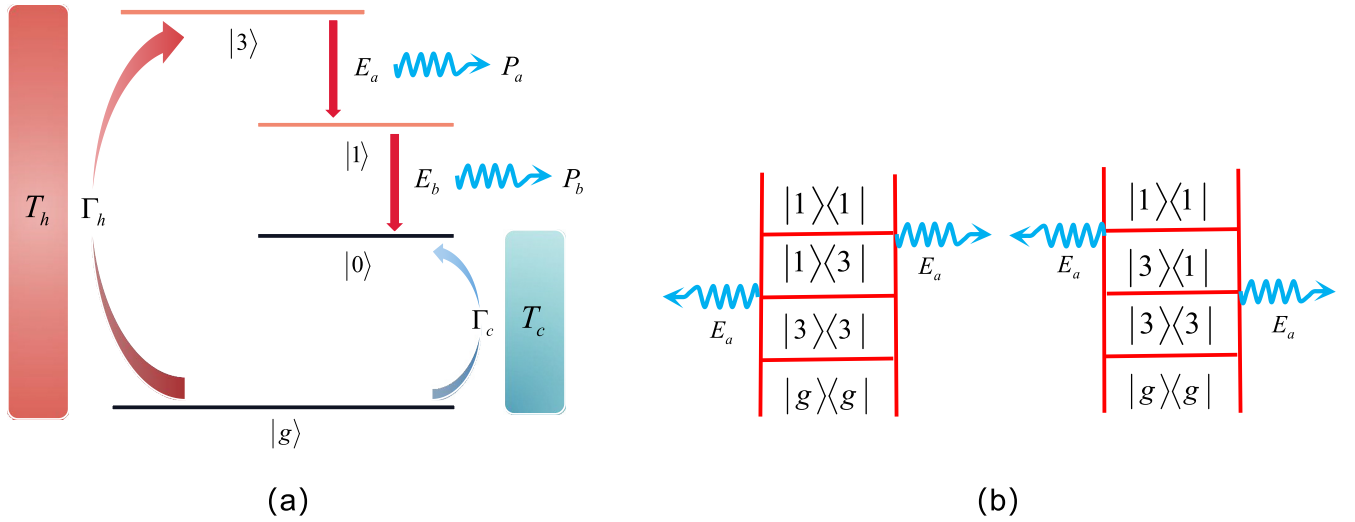
FIG. 5. (a) The schematic of producing power in the incoherently pumped QHE model. E_a and E_b represent two weak single-mode fields driving the respective transitions $3 \to 1$ and $1 \to 0$ resonantly. (b) Two diagrams represent a total of two conjugate pathways contributing to the power P_a in the incoherently pumped model.

where: $V_a = \mu_a |1\rangle\langle 3|$, $V_b = \mu_b |0\rangle\langle 1|$ are the dipole operators and the coefficients $\mu_i (i = a, b)$ are the coupling factors between the system and the light fields. In the interaction picture, the two weak fields with simplified amplitudes ε_a, ε_b are taken as: $\hat{E}_a(t) = \varepsilon_a \hat{a} e^{-i\omega_a t}$, $\hat{E}_b(t) = \varepsilon_b \hat{b} e^{-i\omega_b t}$.

The QHE power can be defined as a rate of change of the averaged probe photon number N multiplied by the corresponding single-photon energy [22,29]. In our analysis, $\hat{N}$ is the photon number operator and the total power for the system at the resonant frequency is:

$$P_{\text{tot}} = P_a + P_b = \hbar\omega_a \frac{d}{dt}\langle \hat{N}_a \rangle + \hbar\omega_b \frac{d}{dt}\langle \hat{N}_b \rangle. \quad (15)$$

Note that the first term P_a mainly depends on the second-order perturbation with respect to light-matter interaction, which corresponds to the system transition $3 \to 1$, while the term P_b mainly depends on the fourth-order perturbation corresponding to the system transition $3 \to 1 \to 0$. Thus, the contribution of P_b can be neglected in the weak coupling regime. Then we can obtain: $P_{\text{tot}} \approx P_a$.

In what follows, only the resonant case is considered $\omega_a = \omega_{31}$. Two diagrams in Fig. 5(b) show a total of two conjugate pathways contributing to the generated power. Using the diagrammatic method outlined in Appendix E and the similar method in Ref. [29], one can easily obtain the steady-state output power in the weak coupling regime as:

$$P_{\text{tot}} = \frac{2\omega_{31}}{\hbar} \varepsilon_a^2 \mu_a^2 \frac{n_h(1 + n_c)}{\Gamma_h(1 + n_h)(1 + 2n_c + 2n_h + 3n_c n_h)}. \quad (16)$$

Here we note the factor $\frac{n_h(1+n_c)}{1+2n_c+2n_h+3n_c n_h}$ is the steady-state value of $\rho_{33}(t)$ in this weak coupling regime and this can be found in Eq. (10). The factor $\Gamma_h(1 + n_h)$ comes from the coherent transition $3 \to 1$ with dissipation, which inhibits the power generation. In the following discussion, we only focus on two typical cases.

In the first case we set $n_h \gg n_c \gg 1$, which corresponds to the high-temperature limit and exhibits high nonclassical correlations (nontrivial peaks) in the output. The corresponding QHE power in this regime yields:

$$P_{\text{tot1}} \approx \frac{2\omega_{31}}{\hbar} \varepsilon_a^2 \mu_a^2 \frac{1}{3\Gamma_h n_h}. \quad (17)$$

In the second case we set $n_c = 0$, which does not show nonclassical correlations (nontrivial peaks) in the output. The corresponding QHE power reads:

$$P_{\text{tot2}} = \frac{2\omega_{31}}{\hbar} \varepsilon_a^2 \mu_a^2 \frac{n_h}{\Gamma_h(1 + n_h)(1 + 2n_h)}$$
$$\leqslant \frac{2\omega_{31}}{\hbar} \varepsilon_a^2 \mu_a^2 \frac{1}{\Gamma_h(3 + 2\sqrt{2})}. \quad (18)$$

Note that the upper bound of the power in Eq. (18) can be achieved when $n_h = 1/\sqrt{2}$, and the corresponding maximum steady-state power is significantly larger than P_{tot1}.

Accordingly, in the high-temperature limit $n_h \gg n_c \gg 1$, one can obtain the highest nonclassical correlations in the output with pronounced photon indistinguishability. On the other hand, this regime is accompanied by the extremely low steady-state power at the resonant frequency since the dissipation at the coherent transition $3 \to 1$ largely inhibits the power generation in the high-temperature limit case. In case $n_c = 0$, the nonclassical correlations (nontrivial peaks) are absent in the output. However, one can achieve higher steady-state QHE power.

The above discussions confirm the fundamental feature of the incoherently pumped QHE that the steady-state resonant power and the nonclassical correlations cannot be maximized simultaneously in the weak coupling regime. In this regime, the advanced ability to produce the nonclassical correlations (nontrivial peaks) is accompanied by the diminished ability to achieve the maximum steady-state resonant power.
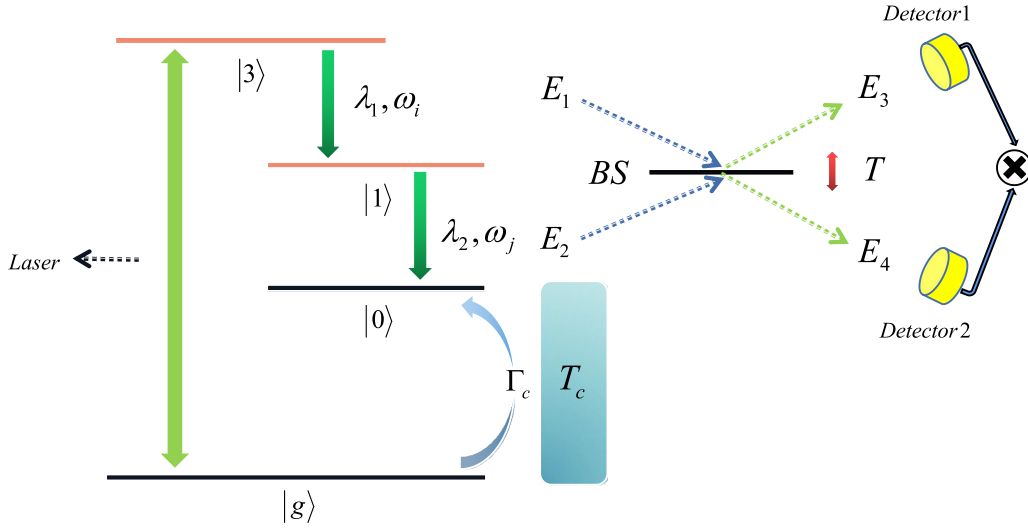
FIG. 6. The schematic of coherently pumped QHE, where the coherent source resonantly drives transition g-3, while the rest of the scheme is identical to the one shown in Fig. 1.

III. COHERENTLY PUMPED QHE MODEL

A. Basic model and PCC signal

So far we have discussed the QHE incoherently pumped by the incoherent thermal field due to its contact with the hot temperature bath. For comparison, we present below the conventional scheme of generating a cascade of correlated photons, which utilizes the coherent source. Figure 6 shows that a coherent pump with finite bandwidth resonantly drives the g-3 transition.

The evolution of the system-matter dynamics in the interaction picture is governed by the density matrix equation:

$$
\begin{aligned}
\frac{\partial \rho}{\partial t} &= \frac{-i}{\hbar}[H_{\text{int}}(t) + H_s, \rho] + \mathcal{L}_c[\rho], \\
H_{\text{int}}(t) &= H_{\text{intqm}}(t) + H_{cl}, \\
H_{\text{intqm}} &= \hat{E}_1^\dagger V_1 + \hat{E}_1 V_1^\dagger + \hat{E}_2^\dagger V_2 + \hat{E}_2 V_2^\dagger, \\
H_{cl} &= E_p^*(t)\lambda_0|g\rangle\langle 3| + E_p(t)\lambda_0|3\rangle\langle g|, \\
\rho(0) &= \rho_s(0) \otimes \rho_{f1}(0) \otimes \rho_{f2}(0).
\end{aligned}
\tag{19}
$$

Compared to Eq. (1) in the incoherently pumped QHE model, Eq. (19) has interaction with only one (cold) bath governed by $\mathcal{L}_c[\rho]$. H_{cl} represents the weak interaction with the classical coherent pump field, and H_{intqm} represents the weak interactions with the two quantum probe fields. The coefficient λ_0 is the coupling factor between the system and the classical coherent pump field. Here, we choose the resonant coherent field $E_p(t) = \theta(t)E_0 e^{-\sigma t - i\omega t}$, where σ denotes the envelope of the coherent field mimicking the single thermal bath dephasing rate for more precise comparison, $\theta(t)$ is the Heaviside step function, $\omega = \omega_{3g}$, and E_0 is the amplitude of the classical pump field.

Following the previous discussions, we can proceed to calculate the PCC by setting $T < 0$ and keep the treatment related to PCC signal $R_c^{34}(t_{c1}, t_{c2})$ in Appendix G. Taking asymptotic value for the $R_c^{34}(t_{c1}, t_{c2})$, we obtain the simplified

steady-state background signal as:

$$
R_c^{34}(\infty, \infty) = \frac{\Gamma_c + \Gamma_c n_c + \sigma}{4\sigma(\Gamma_c n_c + \sigma)(\Gamma_c + 2\Gamma_c n_c + \sigma)\sigma_{T1}\sigma_{T2}}.
\tag{20}
$$

And the corresponding normalized (relative) PCC is given by:

$$
G_c^{(2)}(t_{c1}, t_{c2}) = \frac{R_c^{34}(t_{c1}, t_{c2})}{R_c^{34}(\infty, \infty)}.
\tag{21}
$$

We adopt $\sigma_{T1} = \sigma_{T2}$ in the further analysis and follow the similar set of approximations as in Sec. II C above except that we take $t_{c1} \gg \max\{\frac{1}{2\sigma}, \frac{1}{\Gamma_c n_c + \sigma}\}$ to reduce the nonequilibrium effect of the system related to t_{c1}. Using Eq. (21) and taking $t_{c1} - t_{c2} = -T(T < 0)$, one can obtain the same result for the relative value of the dip as in Eq. (8):

$$
D_c^{\text{ss}} \equiv \min G_c^{(2)}(t_{c1}, t_{c2}) = G_c^{(2)}(t_{c1} - t_{c2} = -T) = e^{T\sigma_{T2}}.
\tag{22}
$$

By taking $t_{c1} = \Gamma_c^{-1}$, considering the detectors with the large temporal bandwidth and fixing the value of $|T|$ to be small, one can obtain simulation of $G_c^{(2)}(t_{c2})$ in Fig. 7. Figure 7 shows that the steady-state regime for the PCC corresponds to the maximum PCC value and highest correlation, which is drastically different from the incoherent pump case shown in Fig. 3(c).

B. Reconstructing the system dynamics using the probe signal

To recover the system dynamics, we first calculate the $\rho_{33}(t)$ (detailed calculations are shown in Appendix G) and only consider the following two cases. Under the condition of nonzero temperature of cold bath with $n_c > 1$ and the large pump envelope $\sigma \gg \Gamma_c(1 + 2n_c)$ corresponding to the strong pump regime in the previous model, we can obtain: $\rho_{33}(t) \approx \frac{(E_0\lambda_0)^2}{\hbar^2\sigma^2}(1 - e^{-t\sigma})^2$. In the zero-temperature limit such that $n_c \to 0$, we can get: $\rho_{33}(t) = \frac{(E_0\lambda_0)^2}{\hbar^2\sigma^2}(1 - e^{-t\sigma})^2$, which is a growing function of time.
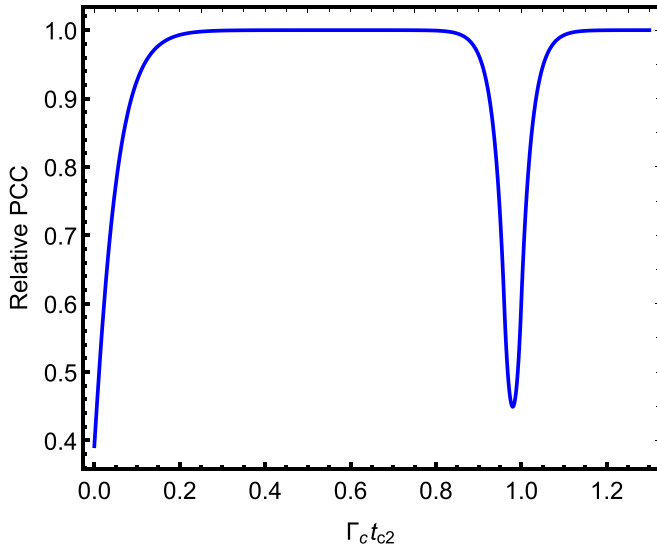
FIG. 7. Normalized (relative) PCC signal for the QHE pumped by a coherent source. Simulations scaled with Γ_c employ the following parameters: $\sigma = 20\Gamma_c$, $\sigma_{T1} = \sigma_{T2} = 40\Gamma_c$, $n_c = 4$, $t_{c1} = 1/\Gamma_c$, $T = -0.02/\Gamma_c$.

Both above two cases show the increasing function depending on t, and the relative value $\rho^c(t)$ similarly defined as Eq. (10) is

$$\rho^c(t) \equiv (1 - e^{-t\sigma})^2. \tag{23}$$

After defining the relative peak value as the maximum value of the population $\rho_{33}(t)$ relative to its steady-state value: $Q_c \equiv \frac{\max_t \rho_{33}(t)}{\rho_{33}(\infty)} = \max_t \rho^c(t)$, the corresponding value is given by: $Q_c = 1$.

Following the similar discussions and approaches as in Sec. II D, one can find the similar relationship between the normalized PCC signal and the population dynamics of level 3 as in Eq. (11):

$$G_c'^{(2)}(t) = \rho^c(t). \tag{24}$$

It is clear that the maximum value of the PCC gradually reaches the steady-state value and there are no additional peak features. After defining the maximum value relative to the steady-state value of the system dynamics, we further define the maximum PCC value relative to the steady-state value: $Q_c^{\mathrm{pcc}} \equiv \max_t G_c'^{(2)}(t)$. Clearly, both maxima are the steady-state value and identical: $Q_c^{\mathrm{pcc}} = Q_c = 1$.

Then the dynamical visibility parameter V_c for fixed t_{c1} in the coherently pumped model can be found as:

$$V_c \equiv \frac{\mathrm{dip}}{\max R_c^{34}(t_{c2})} = \frac{\mathrm{dip}}{R_c^{34}(\infty, \infty)} \frac{R_c^{34}(\infty, \infty)}{\max R_c^{34}(t_{c2})} = \frac{D_c^{\mathrm{ss}}}{Q_c^{\mathrm{pcc}}}. \tag{25}$$

We can obtain the result: $V_c = D_c^{\mathrm{ss}} = e^{T\sigma_{T_2}}$ ($T < 0$). This suggests that the generation of two photons in the steady-state regime yields the maximum correlation and leads to the highest degree of photon indistinguishability, if $T < 0$ and the temporal bandwidth of the detectors is large. This result also shows that the use of the steady-state value for the PCC as the reference is sufficient to precisely reflect the

indistinguishable property of the generated entangled two photons in both nonequilibrium and steady-state regimes. It is important to note that the nonclassical correlations (nontrivial peaks) are absent in the coherently pumped model, unlike the case of the incoherently pumped model.

IV. DISCUSSION AND CONCLUSIONS

Given identical detectors and delay time T ($T < 0$) in the steady-state regime, $D_{\mathrm{inc}}^{\mathrm{ss}} = D_c^{\mathrm{ss}}$ equality is valid. In the nonequilibrium regime, if $n_c = 0$, the visibility of both incoherently and coherently pumped QHEs are identical $V_{\mathrm{inc}} = V_c$. If $n_h \gg n_c \gg 1$, we find that the visibilities are related as $V_{\mathrm{inc}} \leqslant V_c$ and $V_{\mathrm{inc\,min}} = \frac{2}{3}V_c$. The smallest V_{inc} value can be achieved when we consider the high-temperature limit condition and assuming large temporal gate bandwidth $\sigma_T \gg \max\{l_2, l_3\}$ in the incoherently pumped QHE. These results manifest the fact that the two-photon indistinguishability in the nonequilibrium regime for the incoherently pumped QHE can be more pronounced compared to the coherently pumped QHE. These also suggest that the thermal pumping has the potential to highlight the dynamic effects of the nonequilibrium dynamics and generate higher nonclassical correlations in the output work, resulting from the dynamical competition caused by the hot and cold nonzero temperature baths interacting with the system. It is important to note that this dynamical competition is specific to the incoherently pumped QHE model and does not exist in the coherently pumped QHE model.

In summary, we study a four-level quantum heat engine, which generates a cascade of entangled photon pairs, and the correlation statistics of the output work via the two-photon emission can be detected using the intensity-intensity correlation measurement. We show that the photon coincidence counting with carefully designed optical control along with the gated detection can be used to reconstruct the dissipative nonequilibrium dynamics of the incoherently pumped QHE system. Comparing our findings with the coherently pumped model, we find that the thermal pumping has the potential to generate nonclassical correlations (nontrivial peaks) in the output, resulting in photon indistinguishability. This also emphasizes the thermodynamic advantage of the thermal pumping in highlighting the nonequilibrium effects induced by the two nonzero temperature baths. Lastly, we examine the ability of the incoherently pumped QHE to produce the steady-state power at the resonant frequency. Our calculations reveal a fundamental characteristic of the incoherently pumped QHE model: in the weak coupling regime, it is impossible to maximize both the steady-state resonant power and the nonclassical correlations (nontrivial peaks) simultaneously. In this regime, the advanced ability to produce the nonclassical correlations is closely connected with the diminished ability to achieve the maximum steady-state resonant power. Our results suggest that the correlation measurement method provides a novel tool to give insight into the nonequilibrium features of a thermodynamic open quantum system.

APPENDIX A: BASIC TREATMENT OF LIGHT-MATTER INTERACTIONS IN THE INCOHERENTLY PUMPED QHE MODEL

Here we denote the noninteracting Hamiltonians of the QHE system as the following: $H_s = \hbar \sum_i \omega_i |i\rangle\langle i| (i = g, 0, 1, 3)$; $H_{f_1} = \hbar \sum_i \omega_i \hat{a}_i^\dagger \hat{a}_i$; $H_{f_2} = \hbar \sum_j \omega_j \hat{b}_j^\dagger \hat{b}_j$. The H_s represents the system Hamiltonian, and H_{f1}, H_{f2} represent the quantum field 1 and field 2 Hamiltonians, respectively.

We limit all of our discussions to the rotating wave approximation in this work, and the two-photon probe fields-system interaction Hamiltonian is: $H_{\text{int}} = \hat{E}_1^\dagger V_1 + \hat{E}_1 V_1^\dagger + \hat{E}_2^\dagger V_2 + \hat{E}_2 V_2^\dagger$, where: $V_1 = \lambda_1 |1\rangle\langle 3|$, $V_2 = \lambda_2 |0\rangle\langle 1|$ are the dipole operators. The λ_1, λ_2 are the average effective dipole moments. The multimode quantum field 1 and field 2 in quantized volume Ω are given by:

$$\hat{E}_1 = \sum_i \left(\frac{2\pi\hbar\omega_i}{\Omega}\right)^{1/2} \hat{a}_i e^{ik_i r},$$

$$\hat{E}_2 = \sum_j \left(\frac{2\pi\hbar\omega_j}{\Omega}\right)^{1/2} \hat{b}_j e^{ik_j r}. \tag{A1}$$

Here $\hat{a}_i, \hat{b}_j$ represent the Boson operators of quantum field 1, 2. For simplicity, we set $r = 0$, also the average effective dipole moments $\lambda_i (i = 1, 2)$ are assumed to be real.

We assume that the cold and hot baths are very large, and the couplings between the system and the baths are very weak, which means the Born approximation can be taken. Additionally, we assume that the intrinsic time evolution scales of each bath are much shorter than the evolution of the time scale governing the system. In other words, we assume that bath intrinsic correlations decay rapidly [18,19,47,48]. Under these assumptions, the Markov approximation and the Weiskopf-Wigner approximation can be properly used, and then we separately obtain the two dissipative Liouville operators that describe the effects induced by the cold and the hot baths in many works related to the QHE physics [26,33,45]. Accordingly, the cold bath and hot bath can be separately introduced using the Liouville operators as [29]:

$$\mathcal{L}_c[\rho] = \Gamma_c(n_c + 1)(2|g\rangle\langle g|\rho_{00} - |0\rangle\langle 0|\rho - \rho|0\rangle\langle 0|)$$
$$+ \Gamma_c n_c(2|0\rangle\langle 0|\rho_{gg} - |g\rangle\langle g|\rho - \rho|g\rangle\langle g|),$$

$$\mathcal{L}_h[\rho] = \Gamma_h(n_h + 1)(2|g\rangle\langle g|\rho_{33} - |3\rangle\langle 3|\rho - \rho|3\rangle\langle 3|)$$
$$+ \Gamma_h n_h(2|3\rangle\langle 3|\rho_{gg} - |g\rangle\langle g|\rho - \rho|g\rangle\langle g|). \tag{A2}$$

Here the Γ_h, Γ_c are the relaxation factors of the respective two baths and assumed in the same order of magnitude. n_h, n_c are the average photon occupation numbers of hot bath and cold bath respectively given by: $n_h = \{\exp[\hbar\omega_{3g}/(k_B T_h)] - 1\}^{-1}$, $n_c = \{\exp[\hbar\omega_{0g}/(k_B T_c)] - 1\}^{-1}$.

In the interaction picture respect to the optical quantum fields, we can find:

$$\hat{E}_1(t) = \sum_i \left(\frac{2\pi\hbar\omega_i}{\Omega}\right)^{1/2} \hat{a}_i e^{-i\omega_i t} = \sum_i \hat{E}_{1i}(t),$$

$$\hat{E}_2(t) = \sum_j \left(\frac{2\pi\hbar\omega_j}{\Omega}\right)^{1/2} \hat{b}_j e^{-i\omega_j t} = \sum_j \hat{E}_{2j}(t). \tag{A3}$$

Then, we can get: $H_{\text{int}}(t) = \hat{E}_1^\dagger(t)V_1 + \hat{E}_1(t)V_1^\dagger + \hat{E}_2^\dagger(t)V_2 + \hat{E}_2(t)V_2^\dagger$, and the dynamics of the density matrix is governed by:

$$\frac{\partial\rho}{\partial t} = \frac{-i}{\hbar}[H_{\text{int}}(t) + H_s, \rho] + \mathcal{L}_c[\rho] + \mathcal{L}_h[\rho]. \tag{A4}$$

Here, we set $\rho(0) = \rho_s(0) \otimes \rho_{f1}(0) \otimes \rho_{f2}(0)$ at the initial time, and the system is in the ground state. The part in the commutator of the joint density matrix Liouville equation describes the weak quantum light-matter interactions, the other parts represent the bath-induced interactions. The nonperturbated dynamics of the system is governed by the hot and cold baths and described as:

$$\frac{\partial\rho_s}{\partial t} = -\frac{i}{\hbar}[H_s, \rho_s] + \mathcal{L}_c[\rho_s] + \mathcal{L}_h[\rho_s]. \tag{A5}$$

Equation (A5) describes a nonequilibrium dynamical process of the system, which is induced by two different temperature baths [18].

APPENDIX B: TIME-FREQUENCY GATES AND THE PCC SIGNAL RESULT OF THE INCOHERENTLY PUMPED QHE

In calculations, we adopt the exponential time gates and $\theta(t)$ is the Heaviside step function:

$$|F_{t1}(t_1', t_{c1})|^2 = \theta(t_1' - t_{c1})e^{-\sigma_{T1}(t_1' - t_{c1})},$$

$$|F_{t2}(t_2', t_{c2})|^2 = \theta(t_2' - t_{c2})e^{-\sigma_{T2}(t_2' - t_{c2})}. \tag{B1}$$

We omit the frequency gates:

$$F_{f1}(\omega', \overline{\omega_1}) = F_{f2}(\omega'', \overline{\omega_2}) = 1. \tag{B2}$$

In this work, we only present the result when $T < 0$ and also neglect some global constant factors irrelevant to the detectors and baths' degrees of freedom for simplicity (the factors l_2, l_3, r_3, r_4 are defined in Appendix C):

$$R^{34}(t_{c1}, t_{c2}) = U_1(t_{c1}, t_{c2}) + U_2(t_{c1}, t_{c2}), \tag{B3}$$

where:

$$U_1(t_{c1}, t_{c2}) = \frac{M_1 + (M_2 + M_3)\theta(t_{c2} - t_{c1})}{8[1 + 2n_h + n_c(2 + 3n_h)]\sigma_{T2}},$$

$$U_2(t_{c1}, t_{c2}) = \frac{M_4 - r_4 M_5 - r_3 M_6 + r_4 M_7 + r_3 M_8 - M_9}{8[1 + 2n_h + n_c(2 + 3n_h)]}, \tag{B4}$$

$$M_1 = \frac{2e^{(-t_{c1} + t_{c2})\sigma_{T2}}(1 + n_c)n_h}{\sigma_{T1} + \sigma_{T2}} - \frac{r_4 e^{-l_2 t_{c1} + (-t_{c1} + t_{c2})\sigma_{T2}}}{l_2 + \sigma_{T1} + \sigma_{T2}}$$
$$- \frac{r_3 e^{-l_3 t_{c1} + (-t_{c1} + t_{c2})\sigma_{T2}}}{l_3 + \sigma_{T1} + \sigma_{T2}},$$

$$M_2 = -\frac{r_4 e^{-l_2 t_{c1}}}{l_2 + \sigma_{T1}} - \frac{r_3 e^{-l_3 t_{c1}}}{l_3 + \sigma_{T1}} + \frac{r_4 e^{-l_2 t_{c1} + (-t_{c1} + t_{c2})\sigma_{T2}}}{l_2 + \sigma_{T1} + \sigma_{T2}}$$

$$+ \frac{r_4 \sigma_{T2} e^{-l_2 t_{c2} + (t_{c1} - t_{c2})\sigma_{T1}}}{(l_2 + \sigma_{T1})(l_2 + \sigma_{T1} + \sigma_{T2})} + \frac{r_3 e^{-l_3 t_{c1} + (-t_{c1} + t_{c2})\sigma_{T2}}}{l_3 + \sigma_{T1} + \sigma_{T2}},$$

$$M_3 = -\frac{2(1 + n_c)n_h e^{(-t_{c1} + t_{c2})\sigma_{T2}}}{\sigma_{T1} + \sigma_{T2}} - \frac{(-1 + e^{(t_{c1} - t_{c2})\sigma_{T1}})\sigma_{T2}}{\sigma_{T1}(\sigma_{T1} + \sigma_{T2})}$$

$$\times 2(1 + n_c)n_h + \frac{r_3 \sigma_{T2} e^{-l_3 t_{c2} + (t_{c1} - t_{c2})\sigma_{T1}}}{(l_3 + \sigma_{T1})(l_3 + \sigma_{T1} + \sigma_{T2})}$$

$$+ \frac{2(1 + n_c)n_h}{\sigma_{T1} + \sigma_{T2}},$$

$$M_4 = \frac{2n_h(1 + n_c)}{\sigma_{T1}\sigma_{T2}}(e^{(2T + t_{c1} - t_{c2})\sigma_{T1}}A_1 + A_2), \tag{B5}$$

$$M_5 = \frac{e^{B_3}A_1 + e^{l_2(T - t_{c2})}A_2}{\sigma_{T1}(l_2 + \sigma_{T2})},$$

$$M_6 = \frac{e^{B_4}A_1 + e^{l_3(T - t_{c2})}A_2}{\sigma_{T1}(l_3 + \sigma_{T2})},$$

$$M_7 = \frac{e^{B_3}A_1 + e^{B_1}A_2}{(l_2 + \sigma_{T2})(l_2 + \sigma_{T2} + \sigma_{T1})},$$

$$M_8 = \frac{e^{B_4}A_1 + e^{B_2}A_2}{(l_3 + \sigma_{T2})(l_3 + \sigma_{T2} + \sigma_{T1})},$$

$$M_9 = \frac{2n_h(1 + n_c)(e^{(2T + t_{c1} - t_{c2})\sigma_{T1}}A_1 + e^{-(2T + t_{c1} - t_{c2})\sigma_{T2}}A_2)}{(\sigma_{T1} + \sigma_{T2})\sigma_{T2}},$$

$$\tag{B6}$$

$$A_1 = 1 - \theta(2T + t_{c1} - t_{c2}), A_2 = \theta(2T + t_{c1} - t_{c2}),$$

$$B_1 = -l_2 T - l_2 t_{c1} - 2T\sigma_{T2} - (t_{c1} - t_{c2})\sigma_{T2},$$

$$B_2 = -l_3 T - l_3 t_{c1} - 2T\sigma_{T2} - (t_{c1} - t_{c2})\sigma_{T2},$$

$$B_3 = l_2 T - l_2 t_{c2} + 2T\sigma_{T1} + (t_{c1} - t_{c2})\sigma_{T1},$$

$$B_4 = l_3 T - l_3 t_{c2} + 2T\sigma_{T1} + (t_{c1} - t_{c2})\sigma_{T1}. \tag{B7}$$

APPENDIX C: TRANSPORT GREEN'S FUNCTION

The nonequilibrium dynamics induced by the two temperature baths in Eq. (A5) can be correctly described by the Pauli master equations [49]:

$$\dot{\rho}_{ii}(t) = -\sum_{jj} k_{ii,jj}\rho_{jj}(t). \tag{C1}$$

Here, $k_{ii,jj}$ is the population transport matrix element. For $i = j$, the $k_{ii,ii}$ is positive. Whereas $i \neq j$, the $k_{ii,jj}$ is negative. The population transport matrix elements satisfy the population conservation: $\sum_i k_{ii,jj} = 0$.

The evolution of the population terms is governed by the population Green's functions:

$$\rho_{jj}(t) = \sum_{ii} G_{jj,ii}(t)\rho_{ii}(0), \tag{C2}$$

where the $G_{jj,ii}(t)$ is given by:

$$G_{jj,ii}(t) = \sum_n \xi_{jn}^{(R)} D_{nn}^{-1} \exp(-\lambda_n t)\xi_{ni}^{(L)}, \tag{C3}$$

where λ_n is the nth eigenvalue of left and right eigenvector $(\xi_n^{(L)}, \xi_n^{(R)})$ and $D = \xi_L \xi_R$ is a diagonal matrix. Using (A2) and (A5), one can obtain the transport Green's functions used in the incoherently pumped QHE model:

$$G_{33,gg}(t) = \frac{2n_h(1 + n_c) - (r_3 e^{-l_3 t} + r_4 e^{-l_2 t})}{2(1 + 2n_c + 2n_h + 3n_c n_h)}. \tag{C4}$$

Here,

$$r_3 = \frac{n_h[\Gamma_h - \Gamma_c(1 + n_c)(1 + 2n_c) + l_5]}{\sqrt{l_1}},$$

$$r_4 = \frac{n_h[\Gamma_c(1 + n_c)(1 + 2n_c) - l_6]}{\sqrt{l_1}},$$

$$l_5 = 2\Gamma_h n_h + \Gamma_h n_c(3 + 4n_h) + (1 + n_c)\sqrt{l_1},$$

$$l_6 = \Gamma_h[1 + 2n_h + n_c(3 + 4n_h)] - (1 + n_c)\sqrt{l_1}, \tag{C5}$$

$$l_2 = \Gamma_c + \Gamma_h + 2\Gamma_c n_c + 2\Gamma_h n_h - \sqrt{l_1},$$

$$l_3 = \Gamma_c + \Gamma_h + 2\Gamma_c n_c + 2\Gamma_h n_h + \sqrt{l_1},$$

$$l_1 = (\Gamma_c + 2\Gamma_c n_c)^2 + (\Gamma_h + 2\Gamma_h n_h)^2 - l_0,$$

$$l_0 = 2\Gamma_c\Gamma_h[1 + 2n_h + 2n_c(1 + n_h)].$$

Similarly, one can get the population transport Green's function used in the second coherently pumped model as:

$$G_{gg,gg}(t) = \frac{n_c}{1 + 2n_c}(1 + e^{-t(1 + 2n_c)2\Gamma_c}) + \frac{1}{1 + 2n_c}. \tag{C6}$$

APPENDIX D: BARE SIGNALS AND REPRESENTATIONS OF PCC SIGNAL

In the further discussion, we utilize the following Fourier transformation definition:

$$F(\omega) = \int f(t)e^{i\omega t}dt,$$

$$f(t) = \frac{1}{2\pi}\int F(\omega)e^{-i\omega t}d\omega. \tag{D1}$$

Using gating transformation Eq. (4), we can obtain:

$$R^{(34)} = \int dt_1' \int d\tau_1 D^{(1)}(t_{c1}, \bar{\omega}_1; t_1'; \tau_1)$$

$$\times \int dt_2' \int d\tau_2 D^{(2)}(t_{c2}, \overline{\omega_2}; t_2'; \tau_2)$$

$$\times \sum_{s,s'} \sum_{r,r'} \langle \hat{E}_{3r'}^\dagger(t_1' + \tau_1)\hat{E}_{4s'}^\dagger(t_2' + \tau_2)\hat{E}_{4s}(t_2')\hat{E}_{3r}(t_1')\rangle,$$

$$\tag{D2}$$

$$D^{(1)}(t_{c1}, \overline{\omega_1}; t_1', \tau_1) = \int d\omega' \frac{1}{2\pi} e^{-i\omega'\tau_1}|F_{f1}(\omega', \overline{\omega_1})|^2$$

$$\times F_{t1}^*(t_1' + \tau_1, t_{c1})F_{t1}(t_1', t_{c1}), \tag{D3}$$

$$D^{(2)}(t_{c2}, \overline{\omega_2}; t_2', \tau_2) = \int d\omega'' \frac{1}{2\pi} e^{-i\omega''\tau_2}|F_{f2}(\omega'', \overline{\omega_2})|^2$$

$$\times F_{t2}^*(t_2' + \tau_2, t_{c2})F_{t2}(t_2', t_{c2}). \tag{D4}$$

Using Eq. (3), the relation of the output $(\hat{E}_3, \hat{E}_4)$ and input $(\hat{E}_1, \hat{E}_2)$, we can get total signal expression:

$$R^{(34)} = R_1^{34} - R_2^{34} - R_3^{34} + R_4^{34}. \tag{D5}$$

Here, we note the corresponding components are

$$R_1^{34} = \frac{1}{4}\left(\frac{1}{2\pi}\right)^2 \int dt_1' \int dw_1' \int dt_2' \int dw_2' W_D^1(t_{c1}, \overline{\omega_1}; t_1', w_1') W_D^2(t_{c2}, \overline{\omega_2}; t_2', w_2')$$
$$\times \int d\tau_1 \int d\tau_2 e^{-iw_1'\tau_1} e^{-iw_2'\tau_2} \sum_{r,r'} \sum_{s,s'} \langle \hat{E}_{1r'}^\dagger(t_1' + \tau_1) \hat{E}_{2s'}^\dagger(t_2' + \tau_2) \hat{E}_{2s}(t_2') \hat{E}_{1r}(t_1') \rangle, \tag{D6}$$

$$R_2^{34} = \frac{1}{4}\left(\frac{1}{2\pi}\right)^2 \int dt_1' \int dw_1' \int dt_2' \int dw_2' e^{-iw_1'T} e^{iw_2'T} W_D^1(t_{c1}, \overline{\omega_1}; t_1' - T, w_1') W_D^2(t_{c2}, \bar{\omega}_2; t_2' + T, w_2')$$
$$\times \int d\tau_1 \int d\tau_2 e^{-iw_1'\tau_1} e^{-iw_2'\tau_2} \sum_{r,r'} \sum_{s,s'} \langle \hat{E}_{1r'}^\dagger(t_1' + \tau_1) \hat{E}_{2s'}^\dagger(t_2' + \tau_2) \hat{E}_{1s}(t_2') \hat{E}_{2r}(t_1') \rangle, \tag{D7}$$

$$R_3^{34} = \frac{1}{4}\left(\frac{1}{2\pi}\right)^2 \int dt_1' \int dw_1' \int dt_2' \int dw_2' W_D^1(t_{c1}, \bar{\omega}_1; t_1', w_1') W_D^2(t_{c2}, \bar{\omega}_2; t_2', w_2') e^{iw_1'T} e^{-iw_2'T}$$
$$\times \int d\tau_1 \int d\tau_2 e^{-iw_1'\tau_1} e^{-iw_2'\tau_2} \sum_{r,r'} \sum_{s,s'} \langle \hat{E}_{2r'}^\dagger(t_1' + \tau_1) \hat{E}_{1s'}^\dagger(t_2' + \tau_2) \hat{E}_{2s}(t_2') \hat{E}_{1r}(t_1') \rangle, \tag{D8}$$

$$R_4^{34} = \frac{1}{4}\left(\frac{1}{2\pi}\right)^2 \int dt_1' \int dw_1' \int dt_2' \int dw_2' W_D^1(t_{c1}, \overline{\omega_1}; t_1' - T, w_1') W_D^2(t_{c2}, \bar{\omega}_2; t_2' + T, w_2')$$
$$\times \int d\tau_1 \int d\tau_2 e^{-iw_1'\tau_1} e^{-iw_2'\tau_2} \sum_{r,r'} \sum_{s,s'} \langle \hat{E}_{2r'}^\dagger(t_1' + \tau_1) \hat{E}_{1s'}^\dagger(t_2' + \tau_2) \hat{E}_{1s}(t_2') \hat{E}_{2r}(t_1') \rangle, \tag{D9}$$

where:

$$W_D^1(t_{c1}, \bar{\omega}_1; t_1', w_1') = \int d\tau_1 D^{(1)}(t_{c1}, \bar{\omega}_1; t_1', \tau_1) e^{iw_1'\tau_1}, \tag{D10}$$

$$W_D^2(t_{c2}, \bar{\omega}_2; t_2', w_2') = \int d\tau_2 D^{(2)}(t_{c2}, \bar{\omega}_2; t_2', \tau_2) e^{iw_2'\tau_2}. \tag{D11}$$

Then the nongated bare signals can be found as:

$$\sum_{r,r'} \sum_{s,s'} \langle \hat{E}_{1r'}^\dagger(t_1' + \tau_1) \hat{E}_{2s'}^\dagger(t_2' + \tau_2) \hat{E}_{2s}(t_2') \hat{E}_{1r}(t_1') \rangle,$$

$$\sum_{r,r'} \sum_{s,s'} \langle \hat{E}_{1r'}^\dagger(t_1' + \tau_1) \hat{E}_{2s'}^\dagger(t_2' + \tau_2) \hat{E}_{1s}(t_2') \hat{E}_{2r}(t_1') \rangle,$$

$$\sum_{r,r'} \sum_{s,s'} \langle \hat{E}_{2r'}^\dagger(t_1' + \tau_1) \hat{E}_{1s'}^\dagger(t_2' + \tau_2) \hat{E}_{2s}(t_2') \hat{E}_{1r}(t_1') \rangle,$$

$$\sum_{r,r'} \sum_{s,s'} \langle \hat{E}_{2r'}^\dagger(t_1' + \tau_1) \hat{E}_{1s'}^\dagger(t_2' + \tau_2) \hat{E}_{1s}(t_2') \hat{E}_{2r}(t_1') \rangle. \tag{D12}$$

These nongated bare signals contain the pure dynamical evolution information of light-matter interactions.

APPENDIX E: DIAGRAMMATIC METHOD RELATED TO SIGNALS IN THE INCOHERENTLY PUMPED QHE MODEL

We calculate the bare signals in the Liouville space, and the signals can be described as the time-ordered products of the superoperators. For each operator B in the Hilbert space, we associate left superoperator and right superoperator as [50]: $B_L X \equiv BX \quad B_R X \equiv XB$. We also define the commutator superoperator in Liouville space as: $B_- \equiv B_L - B_R$.

We first use the superoperators to represent the signals in the Liouville space and after the time ordering taken into consideration, we should switch back to the ordinary Hilbert space operators to calculate the signals. According to the

above discussion, we can modify our bare signals in the Liouville space:

$$\sum_{r,r',s,s'} \langle \hat{E}_{1r'R}^\dagger(t_1' + \tau_1) \hat{E}_{2s'R}^\dagger(t_2' + \tau_2) \hat{E}_{2sL}(t_2') \hat{E}_{1rL}(t_1') \rangle, \tag{E1}$$

$$\sum_{r,r',s,s'} \langle \hat{E}_{1r'R}^\dagger(t_1' + \tau_1) \hat{E}_{2s'R}^\dagger(t_2' + \tau_2) \hat{E}_{1sL}(t_2') \hat{E}_{2rL}(t_1') \rangle, \tag{E2}$$

$$\sum_{r,r',s,s'} \langle \hat{E}_{2r'R}^\dagger(t_1' + \tau_1) \hat{E}_{1s'R}^\dagger(t_2' + \tau_2) \hat{E}_{2sL}(t_2') \hat{E}_{1rL}(t_1') \rangle, \tag{E3}$$

$$\sum_{r,r',s,s'} \langle \hat{E}_{2r'R}^\dagger(t_1' + \tau_1) \hat{E}_{1s'R}^\dagger(t_2' + \tau_2) \hat{E}_{1sL}(t_2') \hat{E}_{2rL}(t_1') \rangle. \tag{E4}$$

Here, we set the initial state of the system as the ground state g. Using the perturbative diagrammatic method [43,50,51], we can get the required dynamical diagrams of the system dynamics, which meet the requirement of the lowest-order light-matter interactions in the whole detection process. All the required diagrams for the incoherently pumped QHE model are showed in Fig. 8.

APPENDIX F: CALCULATING SIGNALS OF THE INCOHERENTLY PUMPED QHE MODEL

Note that the total signal R^{34} comes from four components as denoted in Eq. (D5). Here we give the derivation of R_1^{34}, and the other components can be calculated similarly. We note Eq. (D6) gives R_1^{34}, and the corresponding bare signal in Liouville space is given by Eq. (E1). The value of bare signal reflects the light-matter interactions without gating. Feynman diagrams (a)–(c), and their complex conjugate in Fig. 8 represent six kinds of quantum dynamical paths contributing to the bare signal. We denote the bare signal resulting from the diagram (a) in Fig. 8 as Y1, diagram (b) in Fig. 8 as Y2, Feynman diagram (c) in Fig. 8 as Y3. Then the results of
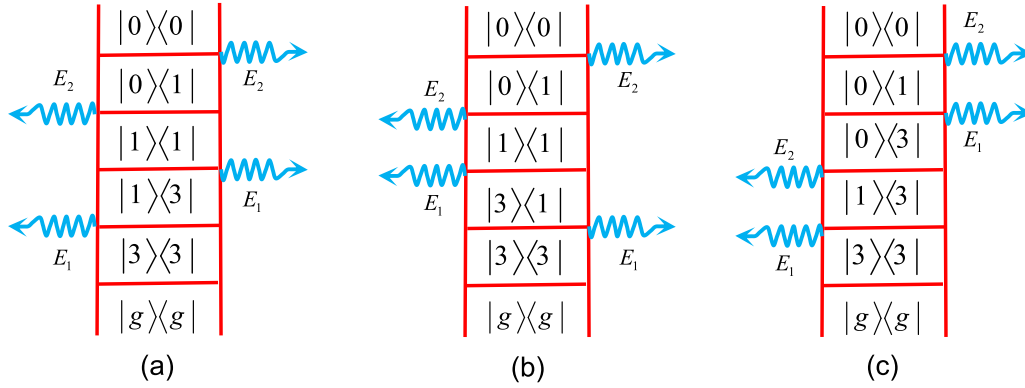
FIG. 8. The double-sided Feynman diagrams represent the pump-probe signal in the whole detection process at the lowest-order light-matter interactions. There are a total of six pathways that contribute to the pump-probe signal of the incoherently pumped QHE model: diagrams (a)–(c), and their complex conjugate.

the bare signal according to the diagrams can be found as the following:

$$Y1 = \sum_{s,s'}\sum_{r,r'} \int_{-\infty}^{t} dt_4 \int_{-\infty}^{t_4} dt_3 \int_{-\infty}^{t_3} dt_2 \int_{-\infty}^{t_2} dt_1 \frac{1}{\hbar^4} \theta(t_2' + \tau_2 - t_4)\theta(t_1' - t_1)\theta((t_1' + \tau_1) - t_2)\theta(t_2' - t_3)$$

$$\times \langle \hat{E}_{1r'R}(t_2)\hat{E}_{2s'R}(t_4)\hat{E}_{1r'R}^{\dagger}(t_1' + \tau_1)\hat{E}_{2s'R}^{\dagger}(t_2' + \tau_2)\hat{E}_{2sL}(t_2')\hat{E}_{1rL}(t_1')\hat{E}_{1rL}^{\dagger}(t_1)\hat{E}_{2sL}^{\dagger}(t_3)\rangle \times \langle V_{2R}^{\dagger}G_{01,01}(t_4 - t_3)V_{2L}$$

$$\times G_{11,11}(t_3 - t_2)V_{1R}^{\dagger}G_{13,13}(t_2 - t_1)V_{1L}G_{33,gg}(t_1)\rangle, \tag{F1}$$

$$Y2 = \sum_{s,s'}\sum_{r,r'} \int_{-\infty}^{t} dt_4 \int_{-\infty}^{t_4} dt_3 \int_{-\infty}^{t_3} dt_2 \int_{-\infty}^{t_2} dt_1 \frac{1}{\hbar^4} \theta(t_2' + \tau_2 - t_4)\theta(t_1' - t_2)\theta((t_1' + \tau_1) - t_1)\theta(t_2' - t_3)$$

$$\times \langle \hat{E}_{1r'R}(t_1)\hat{E}_{2s'R}(t_4)\hat{E}_{1r'R}^{\dagger}(t_1' + \tau_1)\hat{E}_{2s'R}^{\dagger}(t_2' + \tau_2)\hat{E}_{2sL}(t_2')\hat{E}_{1rL}(t_1')\hat{E}_{1rL}^{\dagger}(t_2)\hat{E}_{2sL}^{\dagger}(t_3)\rangle \times \langle V_{2R}^{\dagger}G_{01,01}(t_4 - t_3)V_{2L}$$

$$\times G_{11,11}(t_3 - t_2)V_{1L}G_{31,31}(t_2 - t_1)V_{1R}^{\dagger}G_{33,gg}(t_1)\rangle, \tag{F2}$$

$$Y3 = \sum_{s,s'}\sum_{r,r'} \int_{-\infty}^{t} dt_4 \int_{-\infty}^{t_4} dt_3 \int_{-\infty}^{t_3} dt_2 \int_{-\infty}^{t_2} dt_1 \frac{1}{\hbar^4} \theta(t_2' + \tau_2 - t_4)\theta(t_1' - t_1)\theta((t_1' + \tau_1) - t_3)\theta(t_2' - t_2)$$

$$\times \langle \hat{E}_{1r'R}(t_3)\hat{E}_{2s'R}(t_4)\hat{E}_{1r'R}^{\dagger}(t_1' + \tau_1)\hat{E}_{2s'R}^{\dagger}(t_2' + \tau_2)\hat{E}_{2sL}(t_2').\hat{E}_{1rL}(t_1')\hat{E}_{1rL}^{\dagger}(t_1)\hat{E}_{2sL}^{\dagger}(t_2)\rangle \times \langle V_{2R}^{\dagger}G_{01,01}(t_4 - t_3)$$

$$\times V_{1R}^{\dagger}G_{03,03}(t_3 - t_2)V_{2L}G_{13,13}(t_2 - t_1)V_{1L}G_{33,gg}(t_1)\rangle. \tag{F3}$$

Here we take $t \to \infty$ to get all the nonzero detected signals. If we look at the expression:

$$\sum_{s,s'}\sum_{r,r'}\langle \hat{E}_{1r'R}(t_2)\hat{E}_{2s'R}(t_4)\hat{E}_{1r'R}^{\dagger}(t_1' + \tau_1)\hat{E}_{2s'R}^{\dagger}(t_2' + \tau_2)\hat{E}_{2sL}(t_2')\hat{E}_{1rL}(t_1')\hat{E}_{1rL}^{\dagger}(t_1)\hat{E}_{2sL}^{\dagger}(t_3)\rangle$$

$$= \sum_{s,s',r,r'} \left(\frac{2\pi\hbar\omega_{r'}}{\Omega}\right)\left(\frac{2\pi\hbar\omega_{s'}}{\Omega}\right)\left(\frac{2\pi\hbar\omega_r}{\Omega}\right)\left(\frac{2\pi\hbar\omega_s}{\Omega}\right)e^{-i\omega_{r'}[t_2-(t_1'+\tau_1)]}e^{-i\omega_{s'}[t_4-(t_2'+\tau_2)]}e^{-i\omega_s(t_2'-t_3)}e^{-i\omega_r(t_1'-t_1)}. \tag{F4}$$

Then we approximatively replace the sum with integral considering the multimode fields interaction: $\Sigma_k \to \int \frac{\Omega\omega^2}{\pi^2 c^3}d\omega = \int D(\omega)d\omega$. Using the Weisskopf-Wigner approximation [39,43], we can obtain:

$$D(\omega_s)\left(\frac{2\pi\hbar\omega_s}{\Omega}\right) \approx D(\omega_{10})\left(\frac{2\pi\hbar\omega_{10}}{\Omega}\right),$$

$$D(\omega_r)\left(\frac{2\pi\hbar\omega_r}{\Omega}\right) \approx D(\omega_{31})\left(\frac{2\pi\hbar\omega_{31}}{\Omega}\right).$$

Then we can find Eq. (F4) becomes:

$$= (2\pi)^4 D(\omega_{10})^2 D(\omega_{31})^2 \left(\frac{2\pi\hbar\omega_{31}}{\Omega}\right)^2 \left(\frac{2\pi\hbar\omega_{10}}{\Omega}\right)^2 \delta(t_2 - (t_1' + \tau_1))\delta(t_4 - (t_2' + \tau_2))\delta(t_2' - t_3)\delta(t_1' - t_1).$$

Similarly, we can find:

$$\sum_{s,s'} \sum_{r,r'} \langle \hat{E}_{1r'R}(t_1)\hat{E}_{2s'R}(t_4)\hat{E}_{1r'R}^\dagger(t_1'+\tau_1)\hat{E}_{2s'R}^\dagger(t_2'+\tau_2)\hat{E}_{2sL}(t_2')\hat{E}_{1rL}(t_1')\hat{E}_{1rL}^\dagger(t_2)\hat{E}_{2sL}^\dagger(t_3)\rangle$$

$$= (2\pi)^4 D(\omega_{10})^2 D(\omega_{31})^2 \left(\frac{2\pi\hbar\omega_{31}}{\Omega}\right)^2 \left(\frac{2\pi\hbar\omega_{10}}{\Omega}\right)^2 \delta(t_1-(t_1'+\tau_1))\delta(t_4-(t_2'+\tau_2))\delta(t_2'-t_3)\delta(t_1'-t_2), \quad \text{(F5)}$$

$$\sum_{s,s'} \sum_{r,r'} \langle \hat{E}_{1r'R}(t_3)\hat{E}_{2s'R}(t_4)\hat{E}_{1r'R}^\dagger(t_1'+\tau_1)\hat{E}_{2s'R}^\dagger(t_2'+\tau_2)\hat{E}_{2sL}(t_2')\hat{E}_{1rL}(t_1')\hat{E}_{1rL}^\dagger(t_1)\hat{E}_{2sL}^\dagger(t_2)\rangle$$

$$= (2\pi)^4 D(\omega_{10})^2 D(\omega_{31})^2 \left(\frac{2\pi\hbar\omega_{31}}{\Omega}\right)^2 \left(\frac{2\pi\hbar\omega_{10}}{\Omega}\right)^2 \delta(t_3-(t_1'+\tau_1))\delta(t_4-(t_2'+\tau_2))\delta(t_2'-t_2)\delta(t_1'-t_1). \quad \text{(F6)}$$

Thus, the Y1, Y2, Y3 can be obtained as the following:

$$Y1 = \frac{\pi^4}{\hbar^4} D(\omega_{10})^2 D(\omega_{31})^2 \left(\frac{2\pi\hbar\omega_{31}}{\Omega}\right)^2 \left(\frac{2\pi\hbar\omega_{10}}{\Omega}\right)^2 \langle V_{2R}^\dagger G_{01,01}(\tau_2)V_{2L}G_{11,11}(t_2'-(t_1'+\tau_1))V_{1R}^\dagger G_{13,13}(\tau_1)V_{1L}G_{33,gg}(t_1')\rangle,$$

$$Y2 = \frac{\pi^4}{\hbar^4} D(\omega_{10})^2 D(\omega_{31})^2 \left(\frac{2\pi\hbar\omega_{31}}{\Omega}\right)^2 \left(\frac{2\pi\hbar\omega_{10}}{\Omega}\right)^2 \langle V_{2R}^\dagger G_{01,01}(\tau_2)V_{2L}G_{11,11}(t_2'-t_1')V_{1L}G_{31,31}(-\tau_1)V_{1R}^\dagger G_{33,gg}(t_1'+\tau_1)\rangle,$$

$$Y3 = \frac{\pi^4}{\hbar^4} D(\omega_{10})^2 D(\omega_{31})^2 \left(\frac{2\pi\hbar\omega_{31}}{\Omega}\right)^2 \left(\frac{2\pi\hbar\omega_{10}}{\Omega}\right)^2 \langle V_{2R}^\dagger G_{01,01}(t_2'+\tau_2-(t_1'+\tau_1))V_{1R}^\dagger G_{03,03}(t_1'+\tau_1-t_2')$$

$$\times V_{2L}G_{13,13}(t_2'-t_1')V_{1L}G_{33,gg}(t_1')\rangle. \quad \text{(F7)}$$

We can finally get:

$$R_1^{34} = \frac{1}{4}\left(\frac{1}{2\pi}\right)^2 \int dt_1' \int dw_1' \int dt_2' \int dw_2' W_D^1(t_{c1},\bar{\omega}_1;t_1',w_1')W_D^2(t_{c2},\bar{\omega}_2;t_2',w_2')$$

$$\times \int d\tau_1 \int d\tau_2 e^{-iw_1'\tau_1}e^{-iw_2'\tau_2}(Y1+Y2+Y3) + \text{c.c.} \quad \text{(F8)}$$

Using Eqs. (B1), (B2), (D3), (D4), (D10), (D11), (F7), and (F8), we can obtain the explicit expression of R_1^{34}. Similarly, we can get $R_2^{34}, R_3^{34}, R_4^{34}$. Then the total signal expression can be found according to Eq. (D5) and has been given in Appendix B.

APPENDIX G: BASIC TREATMENT OF LIGHT-MATTER INTERACTIONS IN THE COHERENTLY PUMPED QHE MODEL

The main structure of the total Hamiltonians is the same as the previous case. The modification is the interaction Hamiltonian because we have both classical pump field and quantum probe fields:

$$H_{cl} = E_p^*(t)\lambda_0|g\rangle\langle 3| + E_p(t)\lambda_0|3\rangle\langle g|$$

$$= E_p^*(t)V_g + E_p(t)V_g^\dagger,$$

$$H_{\text{intqm}} = \hat{E}_1^\dagger V_1 + \hat{E}_1 V_1^\dagger + \hat{E}_2^\dagger V_2 + \hat{E}_2 V_2^\dagger. \quad \text{(G1)}$$

The cold bath interaction is introduced the same as in Appendix A. We choose the resonant laser pump pulse with envelope σ and amplitude E_0 as:

$$E_p(t) = \theta(t)E_0 e^{-\sigma t - iwt},$$

$$E_p^*(t) = \theta(t)E_0 e^{-\sigma t + iwt}. \quad \text{(G2)}$$

In the interaction picture respect to the optical quantum fields, we can obtain the total interaction Hamiltonian as:

$$H_{\text{int}}(t) = H_{\text{intqm}}(t) + H_{cl}. \quad \text{(G3)}$$

Under the circumstance of the coherently pumped model, we can find the corresponding dynamical diagrams contributing to $\rho_{33}(t)$ are given in Fig. 9. Then we get the perturbative $\rho_{33}(t)$ to second order:

$$\rho_{33}(t) = \frac{2}{\hbar^2} \text{Re} \int_{-\infty}^t dt_2 \int_{-\infty}^{t_2} dt_1 E_p^*(t_1)E_p(t_2)\langle G_{33,33}(t-t_2)$$

$$\times V_{gL}^\dagger G_{g3,g3}(t_2-t_1)V_{gR}G_{gg,gg}(t_1)\rangle. \quad \text{(G4)}$$

Following the analysis in the incoherently pumped QHE model, we can take the same methods and diagrammatic
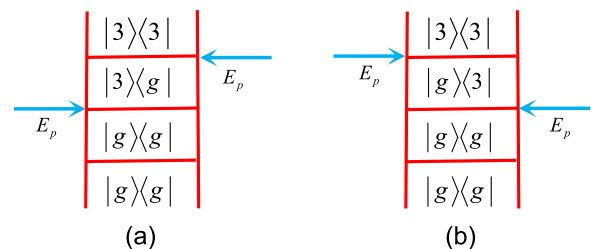

FIG. 9. Two diagrams represent a total of two conjugate pathways contributing to ρ_{33} in the coherently pumped model.
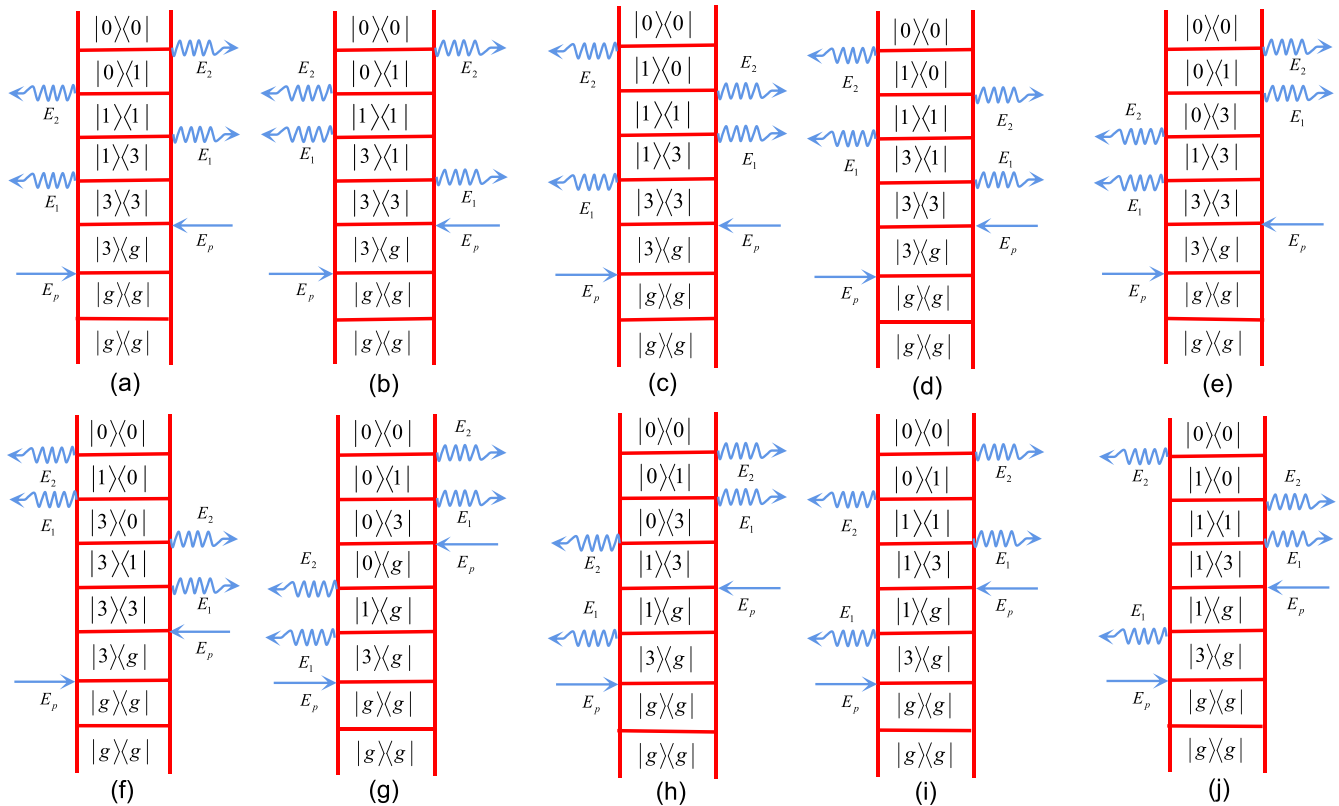
FIG. 10. There are a total of twenty pathways contributing to the pump-probe signal of the coherently pumped QHE model: diagrams (a)–(j), and their complex conjugate.

representation to calculate the PCC signal. All the required independent diagrams related to the coherently pumped case are showed in Fig. 10. There are 20 pathways contributing to the pump-probe signal of the coherently pumped QHE model. Figure 10 shows ten independent diagrams and omits their complex conjugate.

[1] Z. Zhang, T. Peng, X. Nie, G. S. Agarwal, and M. O. Scully, Entangled photons enabled time-frequency-resolved coherent raman spectroscopy and applications to electronic coherences at femtosecond scale, Light Sci. Appl. **11**, 274 (2022).

[2] D. Lago-Rivera, J. V. Rakonjac, S. Grandi, and H. d. Riedmatten, Long distance multiplexed quantum teleportation from a telecom photon to a solid-state qubit, Nature Commun. **14**, 1889 (2023).

[3] J.-W. Pan, Z.-B. Chen, C.-Y. Lu, H. Weinfurter, A. Zeilinger, and M. Żukowski, Multiphoton entanglement and interferometry, Rev. Mod. Phys. **84**, 777 (2012).

[4] T. Jennewein, C. Simon, G. Weihs, H. Weinfurter, and A. Zeilinger, Quantum cryptography with entangled photons, Phys. Rev. Lett. **84**, 4729 (2000).

[5] W. Tittel, J. Brendel, H. Zbinden, and N. Gisin, Quantum cryptography using entangled photons in energy-time bell states, Phys. Rev. Lett. **84**, 4737 (2000).

[6] O. Schwartz, J. M. Levitt, R. Tenne, S. Itzhakov, Z. Deutsch, and D. Oron, Superresolution microscopy with quantum emitters, Nano Lett. **13**, 5832 (2013).

[7] O. Schwartz and D. Oron, Improved resolution in fluorescence microscopy using quantum correlations, Phys. Rev. A **85**, 033812 (2012).

[8] A. Fedrizzi, T. Herbst, M. Aspelmeyer, M. Barbieri, T. Jennewein, and A. Zeilinger, Anti-symmetrization reveals hidden entanglement, New J. Phys. **11**, 103052 (2009).

[9] H. Ta, A. Kiel, M. Wahl, and D.-P. Herten, Experimental approach to extend the range for counting fluorescent molecules based on photon-antibunching, Phys. Chem. Chem. Phys. **12**, 10295 (2010).

[10] K. E. Dorfman, F. Schlawin, and S. Mukamel, Nonlinear optical signals and spectroscopy with quantum light, Rev. Mod. Phys. **88**, 045008 (2016).

[11] D.-I. Lee and T. Goodson, Entangled photon absorption in an organic porphyrin dendrimer, J. Phys. Chem. B **110**, 25582 (2006).

[12] A. R. Guzman, M. R. Harpham, O. Süzer, M. M. Haley, and T. G. Goodson III, Spatial control of entangled two-photon absorption with organic chromophores, J. Am. Chem. Soc. **132**, 7840 (2010).

[13] F. Schlawin, K. E. Dorfman, B. P. Fingerhut, and S. Mukamel, Suppression of population transport and control of exciton distributions by entangled photons, Nature Commun. **4**, 1782 (2013).

[14] H. Oka, Two-photon process via internal conversion by correlated photon pairs, Phys. Rev. A **85**, 013403 (2012).

[15] M. O. Scully and M. S. Zubairy, *Quantum Optics* (Cambridge University Press, Cambridge, 1997).

[16] H. E. D. Scovil and E. O. Schulz-DuBois, Three-level masers as heat engines, Phys. Rev. Lett. **2**, 262 (1959).

[17] R. Alicki, The quantum open system as a model of the heat engine, J. Phys. A: Math. Gen. **12**, L103 (1979).

[18] P. Strasberg, *Quantum Stochastic Thermodynamics: Foundations and Selected Applications* (Oxford University Press, Oxford, 2022).

[19] H.-P. Breuer and F. Petruccione, *The Theory of Open Quantum Systems* (Oxford University Press, Oxford, 2002).

[20] G. Benenti, G. Casati, K. Saito, and R. S. Whitney, Fundamental aspects of steady-state conversion of heat to work at the nanoscale, Phys. Rep. **694**, 1 (2017).

[21] M. Youssef, G. Mahler, and A. S. F. Obada, Quantum optical thermodynamic machines: Lasing as relaxation, Phys. Rev. E **80**, 061129 (2009).

[22] M. O. Scully, K. R. Chapin, K. E. Dorfman, M. B. Kim, and A. Svidzinsky, Quantum heat engine power can be increased by noise-induced coherence, Proc. Natl. Acad. Sci. USA **108**, 15097 (2011).

[23] Y. Yao, Spin-boson theory for charge photogeneration in organic molecules: Role of quantum coherence, Phys. Rev. B **91**, 045421 (2015).

[24] A. A. Svidzinsky, K. E. Dorfman, and M. O. Scully, Enhancing photocell power by noise-induced coherence, Coherent Phenomena **1**, 7 (2012).

[25] K. E. Dorfman, D. V. Voronine, S. Mukamel, and M. O. Scully, Photosynthetic reaction center as a quantum heat engine, Proc. Natl. Acad. Sci. USA **110**, 2746 (2013).

[26] K. E. Dorfman, D. Xu, and J. Cao, Efficiency at maximum power of a laser quantum heat engine enhanced by noise-induced coherence, Phys. Rev. E **97**, 042120 (2018).

[27] Y.-H. Shi, H.-L. Shi, X.-H. Wang, M.-L. Hu, S.-Y. Liu, W.-L. Yang, and H. Fan, Quantum coherence in a quantum heat engine, J. Phys. A: Math. Theor. **53**, 085301 (2020).

[28] M. O. Scully, M. S. Zubairy, G. S. Agarwal, and H. Walther, Extracting work from a single heat bath via vanishing quantum coherence, Science **299**, 862 (2003).

[29] M. Qutubuddin and K. E. Dorfman, Incoherent control of two-photon induced optical measurements in open quantum systems: Quantum heat engine perspective, Phys. Rev. Res. **4**, 023259 (2022).

[30] T. Zhang, W.-T. Liu, P.-X. Chen, and C.-Z. Li, Four-level entangled quantum heat engines, Phys. Rev. A **75**, 062102 (2007).

[31] S. Kamimura, H. Hakoshima, Y. Matsuzaki, K. Yoshida, and Y. Tokura, Quantum-enhanced heat engine based on superabsorption, Phys. Rev. Lett. **128**, 180602 (2022).

[32] H. Wang, S. Liu, and J. He, Thermal entanglement in two-atom cavity QED and the entangled quantum Otto engine, Phys. Rev. E **79**, 041113 (2009).

[33] S.-W. Li, M. B. Kim, G. S. Agarwal, and M. O. Scully, Quantum statistics of a single-atom Scovil–Schulz-DuBois heat engine, Phys. Rev. A **96**, 063806 (2017).

[34] S. Deng, A. Chenu, P. Diao, F. Li, S. Yu, I. Coulamy, A. Del Campo, and H. Wu, Superadiabatic quantum friction suppression in finite-time thermodynamics, Sci. Adv. **4**, eaar5909 (2018).

[35] J. P. S. Peterson, T. B. Batalhão, M. Herrera, A. M. Souza, R. S. Sarthour, I. S. Oliveira, and R. M. Serra, Experimental characterization of a spin quantum heat engine, Phys. Rev. Lett. **123**, 240601 (2019).

[36] J. Klatzow, J. N. Becker, P. M. Ledingham, C. Weinzetl, K. T. Kaczmarek, D. J. Saunders, J. Nunn, I. A. Walmsley, R. Uzdin, and E. Poem, Experimental demonstration of quantum effects in the operation of microscopic heat engines, Phys. Rev. Lett. **122**, 110601 (2019).

[37] M. Qutubuddin and K. E. Dorfman, Incoherent control of optical signals: Quantum-heat-engine approach, Phys. Rev. Res. **3**, 023029 (2021).

[38] C.-K. Hong, Z.-Y. Ou, and L. Mandel, Measurement of subpicosecond time intervals between two photons by interference, Phys. Rev. Lett. **59**, 2044 (1987).

[39] K. E. Dorfman and S. Mukamel, Indistinguishability and correlations of photons generated by quantum emitters undergoing spectral diffusion, Sci. Rep. **4**, 3996 (2014).

[40] K. E. Dorfman and S. Mukamel, Photon coincidence counting in parametric down-conversion: Interference of field-matter quantum pathways, Phys. Rev. A **86**, 023805 (2012).

[41] L. Fleury, J.-M. Segura, G. Zumofen, B. Hecht, and U. P. Wild, Nonclassical photon statistics in single-molecule fluorescence at room temperature, Phys. Rev. Lett. **84**, 1148 (2000).

[42] R. Lettow, Y. L. A. Rezus, A. Renn, G. Zumofen, E. Ikonen, S. Götzinger, and V. Sandoghdar, Quantum interference of tunably indistinguishable photons from remote organic molecules, Phys. Rev. Lett. **104**, 123605 (2010).

[43] K. E. Dorfman and S. Mukamel, Time-and-frequency-gated photon coincidence counting; a novel multidimensional spectroscopy tool, Phys. Scr. **91**, 083004 (2016).

[44] R. Ghosh and L. Mandel, Observation of nonclassical effects in the interference of two photons, Phys. Rev. Lett. **59**, 1903 (1987).

[45] E. Boukobza and D. J. Tannor, Three-level systems as amplifiers and attenuators: A thermodynamic analysis, Phys. Rev. Lett. **98**, 240601 (2007).

[46] A. Muthukrishnan, G. S. Agarwal, and M. O. Scully, Inducing disallowed two-atom transitions with temporally entangled photons, Phys. Rev. Lett. **93**, 093002 (2004).

[47] M. Nakatani and T. Ogawa, Quantum master equations for composite systems: Is Born–Markov approximation really valid? J. Phys. Soc. Jpn. **79**, 084401 (2010).

[48] A. Rivas and S. F. Huelga, *Open Quantum Systems: An Introduction* (Springer, Berlin, 2011).

[49] D. Abramavicius, B. Palmieri, D. V. Voronine, F. Sanda, and S. Mukamel, Coherent multidimensional optical spectroscopy of excitons in molecular aggregates; quasiparticle versus supermolecule perspectives, Chem. Rev. **109**, 2350 (2009).

[50] C. A. Marx, U. Harbola, and S. Mukamel, Nonlinear optical spectroscopy of single, few, and many molecules: Nonequilibrium Green's function QED approach, Phys. Rev. A **77**, 022110 (2008).

[51] S. Mukamel, *Principles of Nonlinear Optical Spectroscopy* (Oxford University Press, Oxford, 1995).